Quantum Correlation-Assisted Cooling of Microwave Cavities Below the Ambient Temperature

Daryoosh Vashaee[a,b*] and Jahanfar Abouie[c]

[a] Department of Materials Science & Engineering, North Carolina State University, Raleigh, NC 27606, USA

[b] Department of Electrical & Computer Engineering, North Carolina State University, Raleigh, NC 27606, USA

[c] Department of Physics, Institute for Advanced Studies in Basic Sciences, Zanjan 45137-66731, Iran

Abstract

We develop a theoretical framework for cooling a microwave cavity mode using a Poisson stream of internally correlated pairs of two-level systems and analyze its performance under realistic dissipation. Starting from a Lindblad model of a phonon-tethered cavity interacting with sequentially injected atom pairs, we derive closed-form expressions for the steady-state cavity occupation and effective temperature. Two coupling geometries are examined: a one-atom configuration, where only one member of each pair interacts with the cavity, and a two-atom configuration, where both atoms couple collectively. The single-atom model enables cooling below the phonon bath but not below the reservoir temperature, whereas the two-atom scheme exhibits enhanced refrigeration - pair correlations modify the cavity's upward and downward transition rates so that the steady-state temperature can fall well below that of the reservoir for weak phonon damping. We map the parameter space including detuning, coupling strength, damping, and intra-pair exchange, identifying cooling valleys near resonance and the crossover between reservoir- and phonon-dominated regimes. The two-atom configuration thus realizes a genuine quantum-enhanced cooling mechanism absent in the single-atom case. We further outline an experimental implementation using two superconducting qubits repeatedly prepared, coupled, and reset inside a 3D cavity. Realistic reset and flux-tuning protocols support MHz-rate interaction cycles, enabling engineered reservoirs to impose cavity temperatures of 50-120 mK even when the cryostat is at ~1 K, offering a pathway to autonomous, on-chip refrigeration of microwave modes in scalable quantum hardware.

Introduction

The rapid growth of quantum information science has placed increasing demands on cryogenic infrastructure for hosting superconducting qubits, microwave resonators, semiconductor spin qubits, and associated control electronics. A central systems-level challenge is the drastic decrease in available cooling power as one descends from kelvin to millikelvin temperatures in a dilution refrigerator. For example, commercial systems typically provide on the order of 10-20 µW at the base ($\approx$ 20 mK) plate, while sub-milliwatt levels are available around 100 mK, and hundreds of milliwatts can be supplied near 1 K.[1,2,3,4,5,6,7] This multi-order-of-magnitude disparity forces nearly all quantum devices onto the coldest stage, where thermal budgets, wiring heat loads, and limited physical space become primary obstacles to scaling.[8,9]

A promising route to alleviating this bottleneck is to relocate as much classical and passive hardware as possible to higher-temperature stages (1-4 K), while using engineered quantum reservoirs to pull selected degrees of freedom, specific cavity modes, qubits, or mesoscopic devices, to effective temperatures far below the ambient of their hosting stage. This idea is firmly rooted in quantum thermodynamics and open quantum systems: collision models, micromaser physics, and quantum thermal machines all show how repeated interactions with small ancilla systems can impose a controlled detailed balance on a target mode and drive it toward a nontrivial steady state.[10,11,12,13,14] In particular, few-body

---

* dvashae@ncsu.edu

quantum refrigerators and absorption machines have been shown theoretically to cool a target system using only finite-size working media.[15,16,17]

A particularly relevant example in this context is the "photo-Carnot" engine of Dillenschneider and Lutz, where a stream of correlated two-level atoms interacts with a single cavity mode and shifts its effective temperature through correlation-modified transition rates.[10] In that model, the cavity acts as a harmonic working medium, while the atomic pairs form a generalized thermal reservoir whose level populations and coherences determine the net heat flow. Under appropriate conditions, the cavity can attain an effective temperature lower than that associated with the atomic populations alone, illustrating how quantum correlations can be harnessed as a thermodynamic resource. Closely related micromaser models, in which individual atoms or atom pairs pass repeatedly through a cavity, have been extensively developed and provide a microscopic foundation for such ancilla-based refrigerators.[14,18,19]

However, the original photo-Carnot formulation and related micromaser models typically neglect coupling to a realistic phonon bath and assume an idealized atomic beam, which complicates direct implementation in microwave hardware. At the same time, circuit quantum electrodynamics (cQED) has matured into a versatile platform for engineering light–matter interactions between high-Q microwave cavities and superconducting qubits.[8,9,20,21,22] In cQED, it is straightforward to realize strong or ultrastrong light–matter coupling, to implement tunable inter-qubit exchange, and to exploit well-developed techniques for state preparation, readout, and dissipation engineering. These capabilities suggest that the role of the atomic beam in the photo-Carnot setup can be played by a small register of superconducting qubits that are repeatedly prepared, interact with the cavity, and are then reset.

In this work we develop and analyze such an architecture. We replace the idealized atomic stream of Ref. [10] with a pair of superconducting qubits that serve as a resettable, correlated reservoir. The qubits repeatedly interact with a high-Q microwave cavity mode and are then actively reset using experimentally demonstrated protocols such as Purcell-enhanced dissipation, measurement-and-feedback reset, or autonomous reservoir engineering.[23,24,25,26,27,28,29,30] The cavity is additionally coupled to a phonon (or thermal) bath at temperature T_{bath}, which we take to lie around 1 K to reflect realistic high-power stages in modern cryogenic systems.[1,2,3,4,5,6] Within this framework, the qubit pair acts as a sacrificial low-entropy working medium, while the cavity is the object to be cooled; the resulting dynamics are naturally described by a collision model with tunable arrival rate, interaction time, detuning, and qubit–qubit correlations.[12]

We first extend the energetics-of-correlations model of Dillenschneider and Lutz [10] by explicitly including cavity-bath coupling and by distinguishing two interaction scenarios: (i) one-subsystem coupling, in which only one atom of the pair couples to the cavity, and (ii) two-subsystem coupling, in which both atoms interact with the cavity field. Using standard input–output and Lindblad techniques,[11,12] we derive closed-form birth-death equations for the cavity photon number that incorporate both the engineered two-qubit reservoir and the phonon bath, and we obtain analytic expressions for the steady-state cavity occupation number and effective temperature. We show how the detailed-balance ratios governing upward and downward transitions depend on the pair's level populations and, when both atoms couple, their mutual coherence; on the strength and duration of each atom–cavity interaction; on atom-cavity detuning; on the arrival rate of pairs; and on the cavity's damping to its phonon bath, thereby generalizing the photo-Carnot temperature shift to a realistic, phonon-tethered setting.

We then evaluate the resulting analytic steady-state expressions over experimentally relevant parameter ranges, focusing on regimes compatible with existing cQED implementations. In particular, we explore how the cavity temperature T_{cav} depends on the atom-cavity coupling g, the inter-qubit exchange coupling λ, the atoms and cavity frequencies detuning Δ, the arrival rate R, and the cavity-bath damping rate κ. We identify broad regions where the engineered reservoir dominates over the 1 K bath and drives the cavity to effective temperatures in the $50 - 20$ mK range, even though the qubit reservoir itself is maintained at an effective temperature $T_{\mathrm{atom}} \approx 30 - 80$ mK by fast reset. In the two-subsystem case, we find that correlations induced by intra-atoms interaction can yield additional cooling relative to the one-subsystem scenario, particularly near resonance, in line with the qualitative predictions of Ref. [10] but now in a fully open-system framework.

Finally, we present a detailed experimental mapping of the proposed refrigerator onto contemporary cQED hardware. We discuss how two transmons or flux-type qubits coupled to a 3D superconducting cavity

can implement the required prepare-interact-reset cycles at MHz rates, making use of established techniques for rapid frequency tuning,[28,47] Purcell-engineered and parametric reset,[26,27,28,29,31] and driven-dissipative state stabilization.[25,32,33,34] We then outline how the cooled cavity mode can in turn be used to refrigerate a target system, such as a gate-defined double quantum dot coupled to the cavity field[35,36] or a secondary cavity mode used as a bosonic memory.[34,37,38,39] In this way, the two-qubit refrigerator operating at a 1 K stage can create a local sub–100-mK environment for selected degrees of freedom without relying on the limited cooling power of the dilution refrigerator's base plate.

The main contributions of this paper are thus: (i) a theoretical extension of the energetics-of-correlations model [10] to include realistic phonon baths and both one- and two-subsystem cavity couplings; (ii) analytic derivation and systematic evaluation of the resulting steady-state cavity temperatures across experimentally relevant parameter regimes; and (iii) a concrete experimental blueprint for realizing a two-qubit photo-Carnot refrigerator in cQED, capable of cooling a cavity mode and, via that mode, a mesoscopic device at a 1 K stage. Together, these results illustrate how quantum correlations and engineered reset protocols can be harnessed to mitigate cryogenic bottlenecks in scalable quantum architectures.

To streamline the presentation in the sections that follow, Table 1 collects all symbols, operators, and rates used in the analysis of the one-atom and two-atom interaction models.

Table 1: Symbols and operators used in the manuscript.

Symbol / Operator	Definition
Fundamental constants and thermodynamic quantities	
$\hbar$	Reduced Planck constant.
k_{B}	Boltzmann constant.
T_{atom}	Temperature used to prepare each correlated two-atom pair in the stream.
T_{bath}	Ambient phonon-bath temperature (substrate temperature).
T_{cav}	Effective cavity temperature defined from Bose inversion of the steady-state photon number (n^*)
β	Inverse temperature, $\beta = 1/(k_{\mathrm{B}} T_{\mathrm{atom}})$
$\bar{n}_1$	Thermal Bose occupation of the phonon bath at ω_1: $\bar{n}_1 = 1/(\exp[\hbar\omega_1/(k_{\mathrm{B}} T_{\mathrm{bath}})] - 1)$.
Frequencies, detuning, Hamiltonians	
ω_1	Cavity angular frequency (single microwave mode).
ω	Single-atom level spacing in the correlated pair.
λ	Intra-pair exchange coupling between the two atoms.
Δ	Atom–cavity detuning: ($\Delta = \omega - \omega_1$).
H	Two-atom pair Hamiltonian: $H = \hbar\omega(\sigma_A^z + \sigma_B^z) + \hbar\lambda(\sigma_A^+ \sigma_B^- + \sigma_A^- \sigma_B^+)$.
H_c	Free cavity Hamiltonian: ($H_c = \hbar\omega_1 a^\dagger a$).
H_{int}	Jaynes–Cummings interaction: ($H_{\mathrm{int}} = \hbar g(a\sigma^+ + a^\dagger \sigma^-)$), with appropriate generalization for two atoms. In general the couplings may differ (g_A, g_B), but here we assume $g_A = g_B \equiv g$.
Operators for cavity and atoms	
$a, a^\dagger$	Cavity annihilation and creation operators.
$\sigma_A^\pm, \sigma_B^\pm$	Ladder operators, respectively, for atom A and atom B in a correlated pair.
$S_\pm$	Collective two-atom ladder operators: ($S_\pm = \sigma_A^\pm + \sigma_B^\pm$).
ρ	Density operator for cavity+atomic pair.

$\mathcal{D}[L]$	Lindblad dissipator: $(\mathcal{D}[L]\rho = L\rho L^{\dagger} - \frac{1}{2}\{L^{\dagger}L, \rho\})$.
$\mathrm{Tr}[\cdot]$	Trace operation.
$\langle\cdot\rangle$	Expectation value with respect to (ρ).
Cavity photon numbers and steady-state quantities	
$n \equiv \langle a^{\dagger}a\rangle$	Cavity photon number.
n^*	Steady-state cavity photon number.
Thermal weights and stream coefficients	
Z	Partition function for the correlated pair: $Z = 2[\cosh(\beta\hbar\omega) + \cosh(\beta\hbar\lambda)]$.
ρ_e, ρ_g	Thermal weights of the single-excitation manifolds: $\rho_e = e^{-\beta\hbar\omega}/Z, \quad \rho_g = e^{\beta\hbar\omega}/Z$
ρ_d, ρ_{nd}	Diagonal and non-diagonal (coherent) pair weights: $\rho_d = \cosh(\beta\hbar\lambda)/Z, \quad \rho_{nd} = -\sinh(\beta\hbar\lambda)/Z$
r_1, r_2	One-subsystem stream coefficients (only one atom couples to cavity photon): $r_1 = \rho_e + \rho_d, r_2 = \rho_g + \rho_d$. Satisfy $r_1 + r_2 = 1$
$r_1^{(2)}, r_2^{(2)}$	Two-subsystem stream coefficients (both atoms couple to cavity photon): $r_1^{(2)} = \rho_e + \rho_d + \rho_{nd}, r_2^{(2)} = \rho_g + \rho_d + \rho_{nd}$. Satisfy, $r_1^{(2)} + r_2^{(2)} = 1 + 2\rho_{nd}$.
Collision / stream parameters	
g	Jaynes–Cummings coupling strength between cavity and atom(s).
τ	Interaction (passage) time per collision.
$\phi \equiv g\tau$	Per-collision interaction angle (assumed $(\varphi \ll 1)$.
$\phi_2^2 \equiv \chi\phi^2$	Effective two-atom coupling strength per collision.
$\chi \in [1,2]$	Coherent enhancement factor for two-atom coupling; $(\chi = 2)$ for fully symmetric coupling.
R	Stream flux (Poisson arrival rate of correlated pairs).
Dissipative rates and cavity cooling parameters	
κ	Cavity-phonon energy-damping rate.
$\kappa^{(\pm)}$	Thermal Lindblad rates: $\kappa^{(-)} = \kappa(\bar{n}_1 + 1), \kappa^{(+)} = \kappa\bar{n}_1$
$\Gamma_{\downarrow}, J_{\uparrow}$	One-subsystem cavity "down/up" coefficients appearing in $\dot{n} = -\Gamma_{\downarrow}n + J_{\uparrow}: \quad \Gamma_{\downarrow} = \kappa + R(r_2 - r_1)\phi^2, J_{\uparrow} = \kappa\bar{n}_1 + Rr_1\phi^2$
$\Gamma_{\downarrow}^{(2)}, J_{\uparrow}^{(2)}$	Two-subsystem analogs with $r_{1,2}^{(2)}$ and ϕ_2^2: $\Gamma_{\downarrow}^{(2)} = \kappa + R(r_2^{(2)} - r_1^{(2)})\phi_2^2; J_{\uparrow}^{(2)} = \kappa\bar{n}_1 + Rr_1^{(2)}\phi_2^2$
$A_{\uparrow}, A_{\downarrow}$	"Birth-death" up/down rates for n_1: $A_{\uparrow} = \kappa\bar{n}_1 + Rr_1^{(2)}\phi_2^2, A_{\downarrow} = \kappa(\bar{n}_1 + 1) + Rr_2^{(2)}\phi_2^2$
Collision maps and Liouvillians	
U	Single-collision unitary: $U = \exp[-(i/\hbar)H_{\mathrm{int}}\tau] \simeq \mathbb{I} - (i/\hbar)H_{\mathrm{int}}\tau - \frac{1}{2\hbar^2}H_{\mathrm{int}}^2\tau^2 + \cdots$
$\Phi(\rho)$	Single-collision map: $\Phi(\rho) = \mathrm{Tr}_{\mathrm{pair}}[U(\rho \otimes \rho_{\mathrm{pair}})U^{\dagger}]$
$\mathcal{L}_{\mathrm{stream}}$	Coarse-grained stream Liouvillian (one-subsystem): $R\phi^2[r_2\mathcal{D}[a] + r_1\mathcal{D}[a^{\dagger}]]$
$\mathcal{L}_{\mathrm{bath}}$	Thermal phonon Liouvillian on cavity: $\kappa^{(-)}\mathcal{D}[a] + \kappa^{(+)}\mathcal{D}[a^{\dagger}]$
Notation conventions	

(·)*	Denotes steady-state value (e.g., n^*).

1. Correlated atom-pair stream: only one atom coupled to a phonon-tethered cavity

1.1 System and parameters

We consider a single bosonic cavity mode a of frequency ω_1, described by the Hamiltonian $H_c = \hbar\omega_1\, a^\dagger a$. The cavity exchanges energy with an ambient phonon bath at temperature T_{bath}, which we model phenomenologically as a thermal Lindblad contact resonant at ω_1 with overall coupling rate κ. The corresponding Bose-Einstein occupation at the cavity frequency is

$$\bar{n}_1 = \frac{1}{\exp\left(\hbar\omega_1/k_B T_{\text{bath}}\right) - 1}. \qquad (1)$$

The cavity is also repeatedly and weakly "kicked" by a stream of *correlated* two two-level atoms that act as an engineered atomic reservoir. Each incoming atom pair is prepared in the thermal state associated with a XY Heisenberg Hamiltonian, characterized by a local splitting $\hbar\omega$ and an exchange coupling $\hbar\lambda$. Writing $\beta \equiv 1/(k_B T_{\text{atom}})$, the state weights in the product basis $\{|ee\rangle, |eg\rangle, |ge\rangle, |gg\rangle\}$ are:[10,18]

$$\rho_e = \frac{e^{-\beta\hbar\omega}}{Z}, \rho_g = \frac{e^{+\beta\hbar\omega}}{Z}, \rho_d = \frac{\cosh\left(\beta\hbar\lambda\right)}{Z}, \rho_{nd} = -\frac{\sinh\left(\beta\hbar\lambda\right)}{Z}, \qquad (2)$$

with the partition function

$$Z = 2[\cosh\left(\beta\hbar\omega\right) + \cosh\left(\beta\hbar\lambda\right)]. \qquad (3)$$

During a short passage of duration τ, only atom A of each atom pair couples (near-resonantly) to the cavity through a Jaynes-Cummings interaction,

$$H_{\text{int}} = \hbar g(a\,\sigma_A^+ + a^\dagger\sigma_A^-), \qquad (4)$$

where $\sigma_A^\pm$ act on atom A. We work in the weak, short-collision (small-angle) limit:

$$\phi \equiv g\tau \ll 1. \qquad (5)$$

The arrivals of independently prepared atom pairs are assumed to follow a Poisson process with rate R, ensuring memoryless, uncorrelated collision events on the coarse-grained timescale.

Because only atom A couples, the local excited state and ground state populations relevant to the cavity dynamics are the marginals of atom A. Evaluating the reduced state of A from Eqs. (2)-(3) yields the effective stream coefficients

$$r_1 = \rho_e + \rho_d, \qquad r_2 = \rho_g + \rho_d, \qquad r_1 + r_2 = 1 \qquad (6)$$

Explicitly,

$$r_2 - r_1 = \frac{e^{\beta\hbar\omega} - e^{-\beta\hbar\omega}}{Z} = \frac{2\sinh(\beta\hbar\omega)}{Z}, \qquad (7)$$

so that correlations (finite λ increasing Z) reduce the effective asymmetry $r_2 - r_1$ at fixed ω, T_{atom}.

1.2 Detuning and the spectral-overlap filter

We now allow a finite detuning between atom (ω) and the cavity (ω_1),

$$\Delta \equiv \omega - \omega_1. \qquad (8)$$

In a single short collision of duration τ, the atom-cavity energy exchange (δE) arises from the overlap of two time/frequency windows: (i) the cavity field correlation, which decays as $\langle a(t)a^\dagger(s)\rangle_{\mathrm{env}} \propto \exp[-(\kappa/2)|t-s|]$ due to its ambient loss channel, and (ii) the finite-time envelope of the atom-cavity interaction, which is nonzero only for $0 \leq t, s \leq \tau$ and therefore has a Fourier width set by $1/\tau$. This can be seen directly by evaluating the second-order term in the single-collision map ($\delta E \propto g^2 \mathrm{Re}\{I(\Delta)\}$), which contains the kernel:[11,12,19]

$$I(\Delta) = \int_0^\tau dt \int_0^\tau e^{-\left(\frac{\kappa}{2}\right)|t-s|}\, e^{i\Delta(t-s)}\, ds \;=\; 2\,\mathrm{Re}\int_0^\tau (\tau - u)\, e^{-\left(\frac{\kappa}{2}-i\Delta\right)u}\, du, \quad (9)$$

The integral has the closed form:

$$I(\Delta) = 2\,\mathrm{Re}\left\{\frac{\tau}{\alpha}(1 - e^{-\alpha\tau}) - \frac{1}{\alpha^2}\left(1 - e^{-\alpha\tau}(1 + \alpha\tau)\right)\right\}, \qquad \alpha \equiv \frac{\kappa}{2} - i\Delta. \quad (10)$$

Two distinct limits are instructive. When $\kappa\tau \gg 1$ (the collision is long compared to the cavity correlation time $2/\kappa$; equivalently, the overlap is cavity-limited), the exponential terms vanish and:

$$I(\Delta) \approx 2\left[\frac{\tau\,(\kappa/2)}{(\kappa/2)^2 + \Delta^2} - \frac{(\kappa/2)^2 - \Delta^2}{((\kappa/2)^2 + \Delta^2)^2}\right] \quad (11)$$

For $\kappa\tau \gg 1$ the τ-independent piece is negligible compared to the τ term, so the leading contribution is:

$$I(\Delta) \approx \frac{\kappa\tau}{(\kappa/2)^2 + \Delta^2} \quad (12)$$

i.e., a Lorentzian in Δ with half width at half maximum (HWHM) $\kappa/2$. This regime corresponds to a relatively low quality factor $Q = \omega_1/\kappa$.

Conversely, when $\kappa\tau \ll 1$ (very short collision), the cavity remains nearly constant over the window, and:

$$I(\Delta) \approx 2\int_0^\tau (\tau - u)\cos(\Delta u)\, du = \frac{\sin^2(\Delta\tau/2)}{\left(\frac{\Delta}{2}\right)^2} = \tau^2 \,\mathrm{sinc}^2\left(\frac{\Delta\tau}{2}\right) \quad (13)$$

whose main lobe has a characteristic width of order $1/\tau$.

Normalizing by $I(\Delta = 0)$ to define the spectral weight actually entering the collision rate, $L(\Delta) \equiv I(\Delta)/I(0)$, the exact lineshape interpolates smoothly between a Lorentzian (cavity-limited) and a sinc^2 (time-window-limited) profile. In the coarse-grained (Markov) generator we retain only the slowly varying secular component; a standard and accurate interpolation is to replace the bare per-collision strength $\phi^2 = (g\tau)^2$ by a Lorentzian detuning filter $L(\Delta)$ whose width is the sum of the two limiting half-widths, namely the cavity homogeneous width and the finite-time Fourier width. With this replacement $\phi^2 \to \phi^2 L(\Delta)$, the detuning simply rescales both the source and slope terms generated by the stream.

Specifically, in a short, weak collision of duration τ, the stream-cavity energy exchange is governed by the overlap of (i) the cavity's Lorentzian line, whose spectral full width at half maximum (FWHM) equals its energy-decay rate κ (since the field correlation decays as $\exp[-(\kappa/2)|t-s|]$), and (ii) the finite-time "window" of the interaction, whose spectral envelope has a main-lobe width of order $1/\tau$ (from the Fourier transform of a length-τ time gate). Evaluating the second-order kernel $I(\Delta)$ yields a closed form that interpolates between a cavity-limited Lorentzian of width κ when $\kappa\tau \gg 1$ (Eq. 12) and a time-window-limited sinc^2 profile of width $\sim 1/\tau$ when $\kappa\tau \ll 1$ (Eq. 13). In the coarse-grained generator we represent this interpolation by a single Lorentzian "overlap" factor,[13]

$$L(\Delta) = \frac{1}{1 + (2\Delta/\Gamma_{\mathrm{over}})^2} \quad (14)$$

with an effective overlap linewidth taken as the sum of the two limiting widths, $\Gamma_{\text{over}} \equiv \kappa + 1/\tau$. This is essentially a detuning filter which replaces the bare ϕ^2. The choice $\Gamma_{\text{over}} = \kappa + 1/\tau$ captures the correct limiting behaviors: for $\tau \to \infty$ (or $\kappa \to \infty$), one recovers $L(\Delta) = 1/[1 + (2\Delta/\kappa)^2]$, while for $\kappa \to 0$, one obtains the expected time-window scaling $L(\Delta) \approx 1/[1 + (2\Delta\tau)^2]$. Small order-unity prefactors that depend on the precise definition of "width" (FWHM vs. HWHM, rectangular vs. smooth window) can be absorbed into Γ_{over} without altering the linear structure of the master equation.

A compact derivation proceeds by expanding the single-collision unitary

$$U = \exp\left[-\frac{i}{\hbar} H_{\text{int}}\tau\right] \simeq \mathbb{I} - \frac{i}{\hbar} H_{\text{int}}\tau - \frac{1}{2\hbar^2} H_{\text{int}}^2 \tau^2 + O(\phi^3), \qquad (15)$$

and evaluating the atom-traced map $\Phi(\rho) = \text{Tr}_{\text{atom}}[U(\rho \otimes \rho_{\text{atom}})U^\dagger]$. The second-order terms involve oscillatory phase factors $e^{\pm i\Delta t}$ from the off-resonant JC coupling and the cavity field correlation $\langle a(t)a^\dagger(0)\rangle \propto e^{-\kappa t/2}$ set by the ambient bath. Integrals of the form:

$$\int_0^\tau dt \int_0^\tau e^{-(\kappa/2)|t-s|} e^{\pm i\Delta(t-s)} ds \qquad (16)$$

yield, after coarse-graining, a Lorentzian detuning profile with sum width equal to the cavity width plus the finite-time Fourier width $1/\tau$. This gives Eq. (14). In the continuous-wave limit $\tau \to \infty$ one recovers the familiar cavity-limited filter $L(\Delta) = 1/[1 + (2\Delta/\kappa)^2]$; conversely, for very short collisions $1/\tau \gg \kappa$ the overlap is dominated by the Fourier width, suppressing off-resonant exchange.

Operationally, the detuning simply rescales the per-collision strength:

$$\phi^2 \longrightarrow \phi^2 L(\Delta) \text{ in all stream-induced terms.} \qquad (17)$$

1.3 Collision model and effective Lindblad generator

With Eq. (17), expanding the one-passage unitary (Eq. (15)) to $\mathcal{O}(\phi^2)$ and tracing over the pair, yields the detuning-dressed one-passage map:

$$\Phi(\rho) \simeq \rho + \phi^2 L(\Delta)[r_2 \mathcal{D}[a]\rho + r_1 \mathcal{D}[a^\dagger]\rho], \qquad (18)$$

where $\mathcal{D}[L]\rho = L\rho L^\dagger - \frac{1}{2}\{L^\dagger L, \rho\}$. For a Poisson train of collisions with rate R, the coarse-grained stream generator is:[14]

$$\mathcal{L}_{\text{stream}}\rho = R\phi^2 L(\Delta)[r_2 \mathcal{D}[a]\rho + r_1 \mathcal{D}[a^\dagger]\rho]. \qquad (19)$$

In parallel, the ambient phonon contact at T_{bath} contributes:

$$\mathcal{L}_{\text{bath}}\rho = \kappa^{(-)}\mathcal{D}[a]\rho + \kappa^{(+)}\mathcal{D}[a^\dagger]\rho, \qquad \kappa^{(-)} = \kappa(\bar{n}_1 + 1), \qquad \kappa^{(+)} = \kappa\bar{n}_1, \qquad (20)$$

which satisfies detailed balance at T_{bath}. The reduced master equation is therefore:

$$\dot{\rho} = \mathcal{L}_{\text{bath}}\rho + \mathcal{L}_{\text{stream}}\rho. \qquad (21)$$

1.4 Photon-number dynamics and cavity effective temperature

Let $n = \langle a^\dagger a\rangle$. Using the standard identities $\text{Tr}[a^\dagger a \, \mathcal{D}[a]\rho] = -n$ and $\text{Tr}[a^\dagger a \, \mathcal{D}[a^\dagger]\rho] = n + 1$, Eq. (21) closes on n as:

$$\frac{dn}{dt} = -\kappa\,(n - \bar{n}_1) + Rr_1\,\phi^2 L(\Delta) - R(r_2 - r_1)\,\phi^2 L(\Delta)n. \qquad (22)$$

It is convenient to define the detuning-dressed damping and injection,[19]

$$\Gamma_{\downarrow}(\Delta) \equiv \kappa + R(r_2 - r_1)\phi^2 L(\Delta), \quad J_{\uparrow}(\Delta) \equiv \kappa\bar{n}_1 + Rr_1\phi^2 L(\Delta), \qquad (23)$$

so that

$$\frac{dn}{dt} = -\Gamma_{\downarrow}(\Delta)\,n + J_{\uparrow}(\Delta). \qquad (24)$$

The solution for any initial $n(0)$ is:

$$n(t) = n^*(\Delta) + [n(0) - n^*(\Delta)]e^{-\Gamma_{\downarrow}(\Delta)t}, \quad n^*(\Delta) = \frac{J_{\uparrow}(\Delta)}{\Gamma_{\downarrow}(\Delta)} = \frac{\kappa\bar{n}_1 + Rr_1\phi^2 L(\Delta)}{\kappa + R(r_2 - r_1)\phi^2 L(\Delta)}. \qquad (25)$$

By modeling the steady state using a Bose-Einstein distribution at frequency ω_1, we obtain the cavity's effective temperature:

$$n^*(\Delta) = \frac{1}{e^{\hbar\omega_1/(k_B T_{cav}(\Delta))} - 1} \Rightarrow T_{cav}(\Delta) = \frac{\hbar\omega_1}{k_B \ln(1 + 1/n^*(\Delta))}. \qquad (26)$$

1.5 Consistency checks and parameter trends

1. Resonant limit. For $\Delta = 0$, $L(0) = 1$ and Eqs. (22)-(26) reduce to the resonant expressions:

$$n(t) = n^* + [n(0) - n^*]e^{-\Gamma_{\downarrow}t}, \ n^* = \frac{\kappa\bar{n}_1 + Rr_1\phi^2}{\kappa + R(r_2 - r_1)\phi^2}, \qquad (27)$$

and

$$T_{cav} = \frac{\hbar\omega_1}{k_B \ln(1 + 1/n^*)}. \qquad (28)$$

2. No stream. If $R\phi^2 \to 0$, then $n^*(\Delta) \to \bar{n}_1$ and the cavity thermalizes to T_{bath}.
3. No phonons. If $\kappa \to 0$, then

$$n^*(\Delta) \xrightarrow{\kappa \to 0} \frac{r_1}{r_2 - r_1}, \qquad (29)$$

independent of Δ, because the cavity line collapses to a delta and the only width in Γ_{over} is $1/\tau$; the common factor $L(\Delta)$ cancels between numerator and denominator in Eq. (25). On resonance this reproduces the one-subsystem stream relation $n^*/(n^* + 1) = r_1/r_2$ and hence

$$e^{-\hbar\omega_1/k_B T_{cav}} = \frac{r_1}{r_2} = \frac{e^{-\beta\hbar\omega} + \cosh(\beta\hbar\lambda)}{e^{\beta\hbar\omega} + \cosh(\beta\hbar\lambda)}, \qquad (30)$$

with $\beta = 1/(k_B T_{atom})$.

4. Large detuning or short dwell. For $|\Delta| \gg \Gamma_{over}$, $L(\Delta) \ll 1$ and the stream's influence is quenched; $n^*(\Delta)$ approaches $\bar{n}_1$. For very short collisions $1/\tau$ dominates Γ_{over}, so $L(\Delta) \approx 1/[1 + (2\Delta\tau)^2]$. There is a natural trade-off: the pump scale grows as $\phi^2 = g^2\tau^2$ but the detuning penalty decreases with larger τ (narrower Fourier width). For fixed g, Δ, κ this produces an optimal τ (hence optimal ϕ) that maximizes the net stream leverage.
5. Role of atom-atom interaction λ. The detuning filter does not modify the bias $r_2 - r_1$, which remains set by $(\omega, T_{atom}, \lambda)$ via Eqs. (2)-(7). Increasing $|\lambda|$ increases Z and thereby weakens the stream's net cooling/heating leverage at any fixed Δ through a smaller $r_2 - r_1$.

1.6 Physical interpretation

The one-subsystem stream provides an incoherent pump at rate $Rr_1\phi^2 L(\Delta)$ (via $\mathcal{D}[a^\dagger]$) and an additional loss channel at rate $Rr_2\phi^2 L(\Delta)$ (via $\mathcal{D}[a]$). Their difference $R(r_2 - r_1)\phi^2 L(\Delta)$ augments the

cavity's damping if $r_2 > r_1$ (cooling tendency) or acts as net gain if $r_1 > r_2$ (heating tendency). The ambient phonon contact fixes the baseline occupation $\bar{n}_1$ and contributes additive damping κ, which guarantees stability even for a slightly inverted stream provided $\kappa > R(r_1 - r_2)\phi^2 L(\Delta)$. The detuning factor $L(\Delta)$ transparently encodes the spectral-overlap physics: cavity losses and finite interaction time both broaden the effective window for exchange (through Γ_{over}), and only the fraction of the stream strength falling inside that window contributes to pumping and damping.

1.7   Validity of the detuned description

The derivation assumes (i) weak, short collisions $\phi = g\tau \ll 1$; (ii) Poissonian arrivals with $R\tau \ll 1$ and finite $R\phi^2$ enabling Markov coarse-graining; (iii) near-resonant coupling and the rotating-wave approximation (RWA) $|\omega - \omega_1| \ll \omega_1$; and (iv) a Born approximation neglecting cavity-stream correlations between collisions. Within this regime, Eqs. (22)-(26) provide a controlled detuned generalization of the resonant one-subsystem result. We note that the choice $\Gamma_{over} = \kappa + 1/\tau$ collects the two relevant broadening mechanisms (cavity damping and finite-time Fourier width) in the simplest additive way. Alternative conventions may differ by order-unity prefactors (e.g., whether one uses FWHM or HWHM for $1/\tau$); such refinements can be absorbed into a calibrated Γ_{over} without altering the linear structure of the theory.

2.   Correlated atom-pair stream: both atoms coupled a phonon-tethered cavity

We return to the collision model of a stream of correlated atom pairs impinging on a single-mode cavity, now allowing both atoms of each pair to couple to the field during their short passage. The cavity remains in contact with an ambient phonon bath at temperature T_{bath}, described exactly as in Section 1 (with bath occupation $\bar{n}_1$ defined in Eq. (1)). The reservoir of correlated pairs is the same as in Section 1: the state weights ρ_e, ρ_g, ρ_d, and ρ_{nd} and the partition function Z are those already introduced in Eqs. (2) and (3).

Each pair interacts with the cavity for a short time τ. For a single atom coupling with strength g, we defined the one-atom small angle $\phi = g\tau \ll 1$. When both atoms couple over the same interval, the net second-order kick on the cavity is enhanced. We parametrize this by an effective per-collision strength

$$\phi_2^2 \equiv \chi\phi^2, 1 \leq \chi \leq 2, \qquad (31)$$

where χ captures geometry and phase: $\chi \simeq 1$ for effectively independent or dephased couplings, and $\chi = 2$ for equal, in-phase, simultaneous couplings that add coherently. Pairs arrive as a Poisson process with flux R (pairs/s).

In order to define the two-subsystem stream coefficients, let $S_\pm \equiv \sigma_A^\pm + \sigma_B^\pm$ denote the collective pair ladders. The second-order collision map depends on the pair correlators $\langle S_+ S_- \rangle$ and $\langle S_- S_+ \rangle$, which evaluate to:[10]

$$r_1^{(2)} = \rho_e + \rho_d + \rho_{nd}, \qquad r_2^{(2)} = \rho_g + \rho_d + \rho_{nd}. \qquad (32)$$

Two useful identities follow immediately:

$$r_2^{(2)} - r_1^{(2)} = \rho_g - \rho_e = \frac{2\sinh(\beta\hbar\omega)}{Z} > 0 \ (\beta\hbar\omega > 0), \qquad r_1^{(2)} + r_2^{(2)} = 1 + 2\rho_{nd}. \qquad (33)$$

As in Section 1, short, weak collisions only "see" the spectral overlap; we therefore use the same detuning filter $L(\Delta)$ defined in Section 1 and simply replace $\phi_2{}^2 \rightarrow \phi_2{}^2 L(\Delta)$ in stream-induced terms.

The one-passage map becomes:

$$\Phi(\rho) \simeq \rho + \phi_2^2 L(\Delta)[r_2^{(2)}\mathcal{D}[a_1]\rho + r_1^{(2)}\mathcal{D}[a_1^\dagger]\rho]. \qquad (34)$$

For a Poisson train of collisions at rate R,

$$\mathcal{L}_{\text{stream}}\rho = R\phi_2^2 L(\Delta)[r_2^{(2)}\mathcal{D}[a_1]\rho + r_1^{(2)}\mathcal{D}[a_1^\dagger]\rho]. \qquad (35)$$

The cavity's ambient phonon contact remains exactly as in Section 1; denoting it by $\mathcal{L}_{\text{bath}}$, the reduced master equation is:

$$\dot{\rho} = \mathcal{L}_{\text{bath}}\rho + \mathcal{L}_{\text{stream}}\rho. \qquad (36)$$

2.1 Effective cavity temperature and limiting cases (two-subsystem)

Parametrizing the steady state by a Bose-Einstein distribution function at ω_1 the cavity's effective temperature is given by,

$$T_{\text{cav}}(\Delta) = \frac{\hbar\omega_1}{k_B \ln\left(1 + 1/n^*(\Delta)\right)}, \qquad (37)$$

where $n^*(\Delta)$ is obtained from Eq. (25) by replacing r_1, r_2, and ϕ respectively with $r_1^{(2)}$, $r_2^{(2)}$, and ϕ_2.

2.2 Limiting cases and trends (two-subsystem)

(i) Resonant limit. For $\Delta = 0$, $L(0) = 1$, and $n^*(\Delta)$ and $T_{\text{cav}}(\Delta)$ reduce to the resonant expressions:

$$n^* = \frac{\kappa\bar{n}_1 + Rr_1^{(2)}\phi_2^2}{\kappa + R(r_2^{(2)} - r_1^{(2)})\phi_2^2} \text{ and } T_{\text{cav}} = \frac{\hbar\omega_1}{k_B \ln(1 + 1/n^*)}.$$

(ii) No phonons: if $\kappa \to 0$, the common factor $L(\Delta)$ cancels,

$$n^*(\Delta) \xrightarrow{\kappa \to 0} \frac{r_1^{(2)}}{r_2^{(2)} - r_1^{(2)}}, \quad \frac{n^*}{n^*+1} = \frac{r_1^{(2)}}{r_2^{(2)}}, \qquad (38)$$

i.e., the two-subsystem stream result independent of detuning.

(iii) No stream: if $R\phi_2^2 \to 0$ (or $L(\Delta) \to 0$ at large $|\Delta|$), $n^*(\Delta) \to \bar{n}_1$ (ambient thermalization).

(iv) Trade-off with τ at fixed g, Δ, κ: the stream leverage scales as $\phi_2^2 \propto \tau^2$ but is penalized by $L(\Delta)$ with $\Gamma_{\text{over}} = \kappa + 1/\tau$; an optimal τ therefore maximizes the net cooling/heating leverage.

(vi) Role of ρ_{nd} and χ: ρ_{nd} shifts both $r_1^{(2)}$ and $r_2^{(2)}$ equally (Eq. 33), biasing the detailed balance colder when $\rho_{nd} < 0$ (e.g., $\lambda > 0$), while χ sets the overall weight of the stream terms through $\phi_2^2 = \chi\phi^2$. The detuning factor $L(\Delta)$ multiplies both pump and slope, transparently encoding spectral mismatch during the finite interaction.

Validity. The derivation assumes weak, short collisions ($\phi = g\tau \ll 1$); Poissonian arrivals with $R\tau \ll 1$ and finite $R\phi_2^2$ enabling Markov coarse-graining; near-resonant coupling and RWA ($|\omega - \omega_1| \ll \omega_1$); and a Born approximation neglecting cavity-stream correlations between collisions. Within this regime, Eq. (37) provides a controlled two-subsystem.

2.3 Physical role of ρ_{nd} and χ (two-subsystem case)

Relative to the one-subsystem configuration, the two-subsystem collision map admits the inter-atomic coherence ρ_{nd} directly into both the upward and downward stream coefficients $r_1^{(2)}$ and $r_2^{(2)}$ (see Eq. (32)). Because ρ_{nd} appears with the same sign in both $r_1^{(2)}$ and $r_2^{(2)}$, it does not modify the net damping bias $r_2^{(2)} - r_1^{(2)}$ (which is fixed solely by the local population asymmetry $\rho_g - \rho_e$ and remains equal to $2\sinh(\beta\hbar\omega)/Z$, cf. Eq. (33)), but it does rescale the absolute magnitude of the stream-induced pump and loss terms. In other words, ρ_{nd} controls how strongly the stream "engages" the cavity without changing the direction (cooling versus heating) set by the population imbalance. When $\rho_{nd} < 0$ (e.g., $\lambda > 0$, antiferromagnetic interaction between atoms in the thermal pair state), both $r_1^{(2)}$ and $r_2^{(2)}$ are lowered relative to the one-subsystem case at the same temperature T_{atom}, biasing the effective detailed balance

colder than T_{cav} for a given collision strength. This cold bias competes with the phonon tether that steadily drags n toward the ambient occupation $\bar{n}_1$ set by T_{bath}.

The geometry/phase factor χ in $\varphi_2^2 = \chi\varphi^2$ (Eq. (31)) quantifies how the second-order "kicks" from the two simultaneous atom-cavity couplings add. For equal-magnitude, in-phase couplings (atoms traversing an antinode with identical phases), χ approaches 2; for geometry or timing that causes partial cancellation or independent addition, $1 \leq \chi < 2$. Since the stream Liouvillian enters as $R\varphi_2^2 L(\Delta)[r_2^{(2)}\mathcal{D}[a] + r_1^{(2)}\mathcal{D}[a^\dagger]]$ (Eq. (35)), χ sets the overall weight of the stream terms multiplicatively with the detuning filter $L(\Delta)$. At finite detuning $\Delta \neq 0$, the spectral-overlap factor $L(\Delta)$ defined in Section 1 multiplies both the upward and downward channels equally, so detuning does not alter the bias $r_2^{(2)} - r_1^{(2)}$ either; instead, $L(\Delta)$ reduces the effective engagement of the stream by the common factor $0 \leq L(\Delta) \leq 1$. Consequently, the net damping and injection that appear in the photon-number equation are both dressed by the same $\chi L(\Delta)$ multiplier through $\varphi_2^2 L(\Delta)$, while the relative bias between them is still controlled entirely by $r_2^{(2)} - r_1^{(2)}$. This separation of roles is useful experimentally: χ is engineering-controlled (mode shape, trajectory, phase), $L(\Delta)$ is spectroscopy-controlled (detuning and the overlap width Γ_{over}), and $r_2^{(2)} - r_1^{(2)}$ is thermodynamics-controlled ($\omega, T_{\text{atom}}, \lambda$ through Z).

Detuning also introduces a practical trade-off with the dwell time τ. Increasing τ increases $\varphi^2 = g^2\tau^2$ and therefore $\varphi_2^2 = \chi g^2\tau^2$, but it simultaneously narrows the time-window contribution to the overlap width, $\Gamma_{\text{over}} = \kappa + 1/\tau$ (Section 1), which increases $L(\Delta)$ for any fixed Δ because the Lorentzian denominator $1 + (2\Delta/\Gamma_{\text{over}})^2$ shrinks when Γ_{over} grows. Thus, for fixed $g, \Delta,$ and κ there is an optimal τ that maximizes the combined leverage $\chi\varphi^2 L(\Delta)$. In the regime where $\kappa\tau \gg 1$, $\Gamma_{\text{over}} \simeq \kappa$ and $L(\Delta)$ is governed by the cavity line; in the opposite regime $\kappa\tau \ll 1$, $\Gamma_{\text{over}} \simeq 1/\tau$ and $L(\Delta) \sim 1/[1 + (2\Delta\tau)^2]$. In both regimes, ρ_{nd} and χ act only as amplitude multipliers (through $r_1^{(2)}, r_2^{(2)}$ and through φ_2^2), while $L(\Delta)$ acts as a spectroscopic gate that uniformly attenuates stream-induced pump and loss.

Finally, stability considerations in the detuned two-subsystem model are transparent in the grouped coefficients: the net damping is $\Gamma_\downarrow^2(\Delta) = \kappa + R\left(r_2^{(2)} - r_1^{(2)}\right)\varphi_2^2 L(\Delta)$. Because $r_2^{(2)} - r_1^{(2)} > 0$ for $\beta\hbar\omega > 0$ (Eq. (33)), detuning cannot invert the stream; it only scales its strength. Hence $\Gamma_\downarrow^2(\Delta)$ remains strictly positive for any Δ, with the phonon contact guaranteeing stability and setting a baseline relaxation even when χ is large and $L(\Delta) \simeq 1$.

2.4 Evaluation workflow for the analytic steady-state (two-subsystem case)

Given the pair thermodynamics $(T_{\text{atom}}, \lambda, \omega)$, first compute the state weights ρ_e, ρ_g, ρ_d, and ρ_{nd} and the partition function Z as in Section 1. From these, form the two-subsystem stream coefficients via Eq. (32): $r_1^{(2)} = \rho_e + \rho_d + \rho_{nd}$ and $r_2^{(2)} = \rho_g + \rho_d + \rho_{nd}$. Next, specify the cavity frequency ω_1 and the ambient temperature T_{bath} to obtain the bath occupation $\bar{n}_1 = 1/[\exp(\hbar\omega_1/k_B T_{\text{bath}}) - 1]$. Choose the collision parameters g and τ, which set the one-atom small angle $\varphi = g\tau$ and the two-atom enhancement $\varphi_2^2 = \chi\varphi^2$ via Eq. (31), with χ determined by geometry and phase. Fix the stream flux R (pairs/s) and the cavity-phonon rate κ.

To introduce the spectroscopic parameters for detuning, pick the single-atom transition ω_{atom} (the same ω used in the pair thermodynamics assuming that the atom that couples has the local gap $\hbar\omega$) and set the detuning Δ. With τ and κ specified, evaluate the effective overlap width $\Gamma_{\text{over}} = \kappa + 1/\tau$ (defined in Section 1) and the detuning filter $L(\Delta) = 1/[1 + (2\Delta/\Gamma_{\text{over}})^2]$. At this point, all ingredients entering the photon-number dynamics are known.

Compute the detuning-dressed damping and injection from Equations: $\Gamma_\downarrow^{(2)}(\Delta) = \kappa + R\left(r_2^{(2)} - r_1^{(2)}\right)\varphi_2^2 L(\Delta)$ and $J_\uparrow^{(2)}(\Delta) = \kappa\bar{n}_1 + R\, r_1^{(2)}\phi_2^2 L(\Delta)$. Insert these into Eq. (24) to obtain the linear birth-death evolution for $n(t)$; the steady state is given in closed form as $n^*(\Delta) = [\kappa\bar{n}_1 + R r_1^{(2)}\phi_2^2 L(\Delta)]/[\kappa + R(r_2^{(2)} - r_1^{(2)})\phi_2^2 L(\Delta)]$. From $n^*(\Delta)$, recover the effective cavity temperature via Eq. (37): $T_{\text{cav}} = \hbar\omega_1/[k_B\ln(1 + 1/n_1^*)]$.

This pipeline makes explicit how each physical knob enters: (i) thermodynamics $(T_{\text{atom}}, \lambda, \omega) \to r_1^{(2)}, r_2^{(2)}$ through Z; (ii) geometry and timing (χ, τ) and coupling strength $g \to \varphi_2^2$; (iii) spectroscopy $(\Delta, \Gamma_{\text{over}}) \to L(\Delta)$; and (iv) environment $(\kappa, T_{\text{bath}}) \to$ baseline damping and occupation. In the limit $\Delta \to 0, L(\Delta) \to 1$, recovering the resonant formulas as a special case without changing any step of the workflow. Conversely, for $|\Delta| \gg \Gamma_{\text{over}}, L(\Delta) \ll 1$ and the stream's influence is strongly attenuated, driving $n^*(\Delta)$ toward $\bar{n}_1$; this suppression can be partially offset by increasing χ or τ, but only within the constraint that $\varphi = g\tau \ll 1$ and $R\tau \ll 1$ remain valid for the collisional coarse-graining. If one wishes to revert to the one-subsystem counterpart while retaining the phonon bath and detuning, simply replace $r_{1,2}^{(2)} \to r_{1,2}$ (thereby dropping ρ_{nd} from the coefficients) and set $\varphi_2^2 \to \varphi^2$; the detuning filter $L(\Delta)$ and the ambient terms remain unchanged.

3. Results and Discussions

All results presented in Figures 1–5 and 7 follow from direct evaluation of the closed-form analytic expressions for the steady-state photon number derived in Sections 1 and 2. To ensure consistency across parameter sweeps, a common baseline parameter set is adopted and summarized in Table 2. These values, representative of contemporary circuit-QED devices, place the system firmly within the weak-collision regime $(\phi = g\tau \ll 1)$ and provide a realistic reference point for assessing cooling performance as individual parameters (detuning, cavity–bath coupling, atom–cavity strength, and pair correlations) are varied.

Table 2: Global Baseline Parameters Used in Analytical Evaluations

Quantity	Symbol / Definition	Value	Notes
Bath temperature	T_{bath}	10 K	Cryogenic stage (phonon environment)
Atomic (two-qubit) temperature	T_{atom}	50 mK	Effective temperature of the engineered reservoir
Cavity frequency	$\omega_1/2\pi$	5 GHz	Fundamental cavity mode
Atom–cavity interaction time	τ	50 ns	Set by flux-pulse duration
Collision (arrival) rate	R	5×10^6 1/s	Mean pair-arrival frequency
Inter-qubit coupling	λ	5 GHz	Exchange coupling between qubits
Jaynes–Cummings coupling	$g/2\pi$	0.5 GHz	Coherent qubit–cavity interaction strength
Cavity–bath damping rate	κ	10 kHz	Moderately weak phonon tether
Collision angle	$\phi = g\tau$	$\phi \approx 0.16$	Ensures weak-collision limit ($\phi \ll 1$)

3.1 Cooling-heating crossover induced by atom-cavity detuning

Figure 1 (a) and (b) summarize the central mechanism by which a correlated atom stream modifies the steady-state temperature of a phonon-tethered cavity. The key control parameter is the detuning $\Delta = \omega - \omega_1$, which governs both the efficiency and directionality of energy exchange between the incoming atomic state and the cavity mode. Because the single-interaction rotation angle $\phi = g\tau \ll 1$ places the system firmly in the weak-collision regime, the effect of each atomic pair on the cavity is additive and can be described by an effective birth–death process for the cavity photon number $n^*(\Delta)$.

As shown in Figure 1 (a), the ratio $T_{\text{cav}}/T_{\text{atom}}$ for the one-atom interaction model exhibits a shallow minimum near $\Delta \approx 0$. This behavior reflects the Lorentzian spectral-overlap filter derived analytically in $n^*(\Delta)$, Eq. (14), which weights the stream-driven absorption and emission processes. Near resonance, the cavity efficiently absorbs entropy-carrying excitations from the incoming atom pairs, and the stream-induced detailed balance

$$\frac{A_\uparrow}{A_\downarrow - A_\uparrow} = \frac{n^*}{1 + n^*}$$

with $A_\uparrow(\Delta) = \kappa \bar{n}_1 + R\, r_1^{(2)} \phi_2^2 L(\Delta)$, $A_\downarrow(\Delta) = \kappa(\bar{n}_1 + 1) + R r_2^{(2)} \phi_2^2 L(\Delta)$, becomes dominant over the intrinsic phonon-bath contribution. As a result, the cavity is pulled toward the effective temperature imposed by the correlated stream, lowering T_{cav} significantly below the phonon-bath temperature.
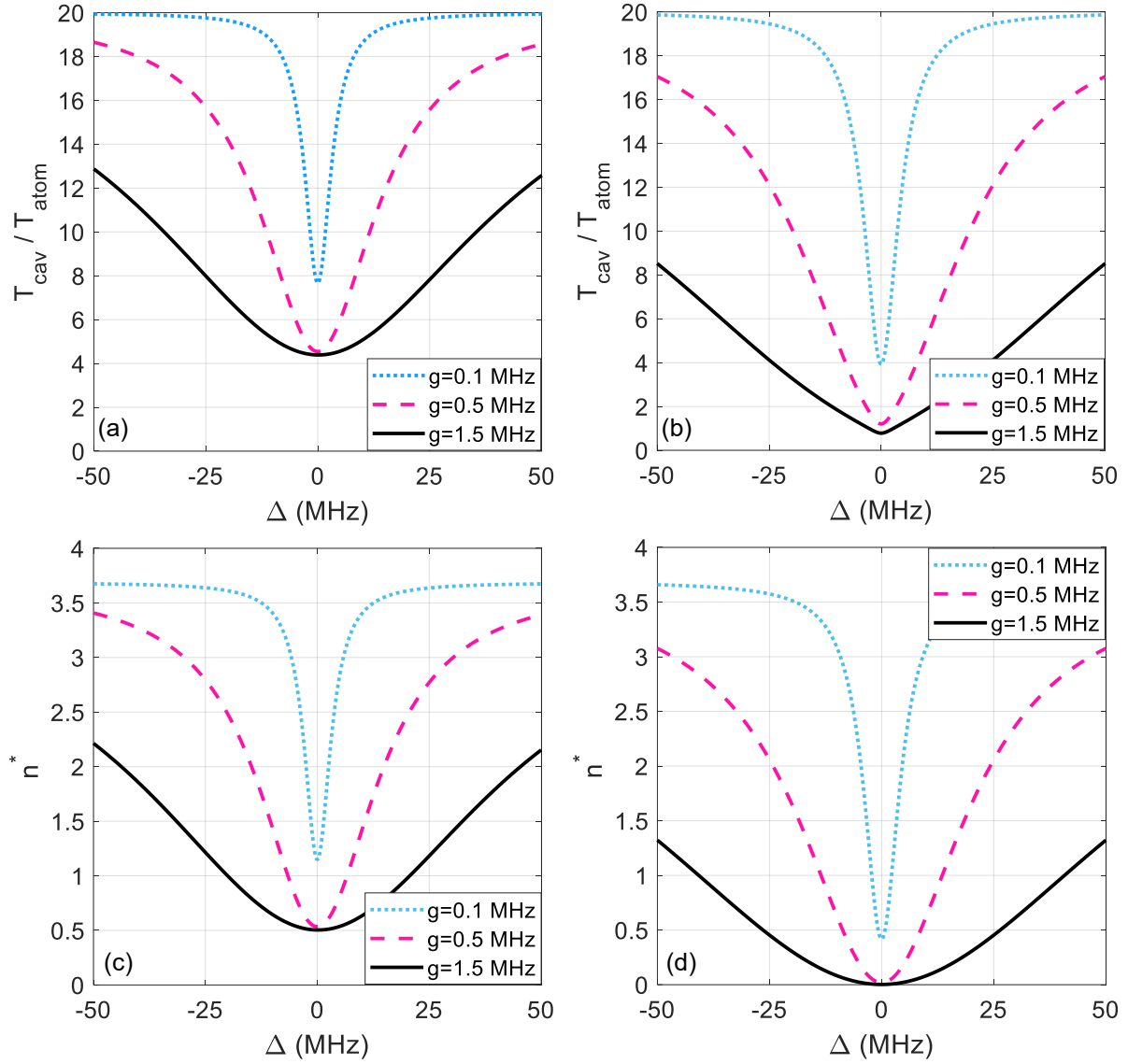
Figure 1: (a,b) Effective cavity temperature versus atom-cavity detuning. The ratio T_{cav}/T_{atom} is shown as a function of the detuning $\Delta = \omega - \omega_1$ for one-atom (a) and two-atom (b) interaction models. Near resonance ($\Delta = 0$), the correlated atom-pair reservoir efficiently exchanges energy with the cavity and drives it toward the reservoir's temperature. For large detuning, the coherent exchange channel is suppressed, the phonon bath dominates, and the cavity warms, yielding $T_{cav} > T_{atom}$. Three representative coupling strengths g are shown in each panel, demonstrating stronger cooling for larger g. In the one-atom case (a), the minimum T_{cav}/T_{atom} remains above unity, approaching a value near ~ 4. In contrast, in the two-atom case (b), T_{cav}/T_{atom} falls below unity, reaching values near ~ 0.5 near resonance and for stronger coupling, indicating genuine refrigeration of the cavity below the atom temperature. (c,d) Steady-state cavity photon number versus detuning. The steady-state cavity occupation n^* is plotted for the same parameters as in (a) and (b), for the one-atom (c) and two-atom (d) models respectively. The detuning dependence reflects the spectral overlap between the atom and cavity modes: efficient near resonance, resulting in reduced photon populations, and suppressed at large detuning, where the cavity relaxes toward the phonon bath. The behavior of $n^*(\Delta)$ corresponds directly to the cooling and heating trends observed in panels (a) and (b).

For detunings $|\Delta| \gtrsim \Gamma_{over}$, the stream–cavity energy exchange (δE) is strongly suppressed and $L(\Delta) \to 0$, such that the steady state population n^* reduces to the phonon-tethered value $n^* \to \bar{n}_1$. This produces the symmetric heating wings observed in Figure 1 (a): because the stream no longer removes sufficient

entropy to compensate bath-induced excitations, the cavity relaxes toward the hotter phonon bath. Thus, the cooling-heating profile as a function of detuning is an intrinsic consequence of spectral filtering imposed by the weak-collision channel.

The influence of the coupling strength g is highlighted in Figure 1 (a). Increasing g enhances the per-collision rotation $g\tau$, thereby amplifying the stream-induced Lindblad rates $R\phi^2 r_1$ and $R\phi^2(r_2 - r_1)$. Physically, this enlarges the domain in which the atomic stream overcomes phonon-bath heating. As g increases, the minimum of $T_{\mathrm{cav}}/T_{\mathrm{atom}}$ becomes increasingly pronounced, and efficient cooling persists out to larger values of detuning. This behavior is consistent with the analytic scaling in Eq. (25), which interpolates between a bath-dominated steady state when $g\tau \to 0$ and a stream-dominated regime when $g\tau$ is sufficiently large for the engineered reservoir to dictate the detailed balance.

Figure 1 (b) also reveals the qualitative enhancement provided by the two-atom interaction model, where both members of the correlated pair couple to the cavity. Here the effective upward/downward rates depend on the two-subsystem coefficients $\left(r_1^{(2)}, r_2^{(2)}\right)$, which incorporate pair coherence more strongly than in the one-atom scenario. As a result, the cavity can be cooled below the temperature of the atomic reservoir itself, with $T_{\mathrm{cav}}/T_{\mathrm{atom}}$ approaching values as low as ~ 0.5 near resonance for strong coupling. The cooling region is also broader: the two-qubit reservoir maintains dominance over the phonon bath across a wider detuning interval, reflecting its stronger collective interaction with the cavity.

Figure 1 (c) and (d) plot the corresponding steady-state photon number $n^*(\Delta)$ for the one-atom and two-atom cases, respectively. The photon-number trends mirror the temperature behavior: in Figure 1 (c), the minimum of n^* is modest and remains above the stream-imposed value, whereas in Figure 1 (d) the cavity photon population is strongly suppressed near resonance, consistent with the significantly deeper cooling achieved in the two-atom configuration. The close correspondence between $n^*(\Delta)$ and $T_{\mathrm{cav}}/T_{\mathrm{atom}}$ across panels (a-d) confirms that the enhanced refrigeration in the two-atom case arises entirely from the modified detailed-balance ratios encoded in the correlated-pair coefficients, rather than from any additional dissipative mechanism.

Together, Figure 1 (a–d) reveal the essential physics of both the one-subsystem and two-subsystem models. In the one-atom case, panels (a) and (c) show that the cavity temperature is governed by a competition between (i) resonant entropy extraction by the correlated atomic stream and (ii) thermal injection from the phonon bath. Detuning suppresses the former through the Lorentzian spectral filter $L(\Delta)$, while increasing coupling g strengthens it by enhancing the stream-induced Lindblad rates $R\phi^2 r_1$ and $R\phi^2(r_2 - r_1)$. As a result, the cooling minimum at $\Delta = 0$ marks the operational "sweet spot" of the refrigerator, where the stream imposes a nonequilibrium detailed balance that can pull the cavity temperature significantly below that of the phonon reservoir, though still above the atom-stream temperature T_{atom}.

In contrast, panels (b) and (d) highlight the two-atom interaction case, where both constituents of the correlated pair couple to the cavity. The collective interaction modifies the effective upward–downward rates via the two-subsystem coefficients $\left(r_1^{(2)}, r_2^{(2)}\right)$, enabling a substantially deeper cooling window. At resonance, the engineered reservoir is strong enough to impose a detailed balance colder than the atomic reservoir itself, allowing T_{cav} to drop below T_{atom} with minima near $T_{\mathrm{cav}}/T_{\mathrm{atom}} \sim 0.5$. This enhanced cooling capability is a direct manifestation of pair coherence and collective emission physics, which broaden the detuning range over which the stream dominates over the phonon bath. Consequently, while the one-atom model demonstrates stream-assisted refrigeration of a phonon-tethered cavity, the two-atom model reveals a qualitatively stronger regime in which correlations within each incoming atomic pair enable genuine quantum-enhanced refrigeration.

3.2 Competition between phonon heating and stream-induced cooling

Figure 2 (a–d) illustrates how the cavity steady state emerges from a competition between two distinct energy-exchange channels: (i) thermalization with the environmental phonon bath, and (ii) entropy extraction by the correlated atomic reservoir. The relative strength of these channels determines whether the cavity is ultimately pulled toward the hot phonon bath or toward the colder effective temperature imposed by the engineered atom stream.
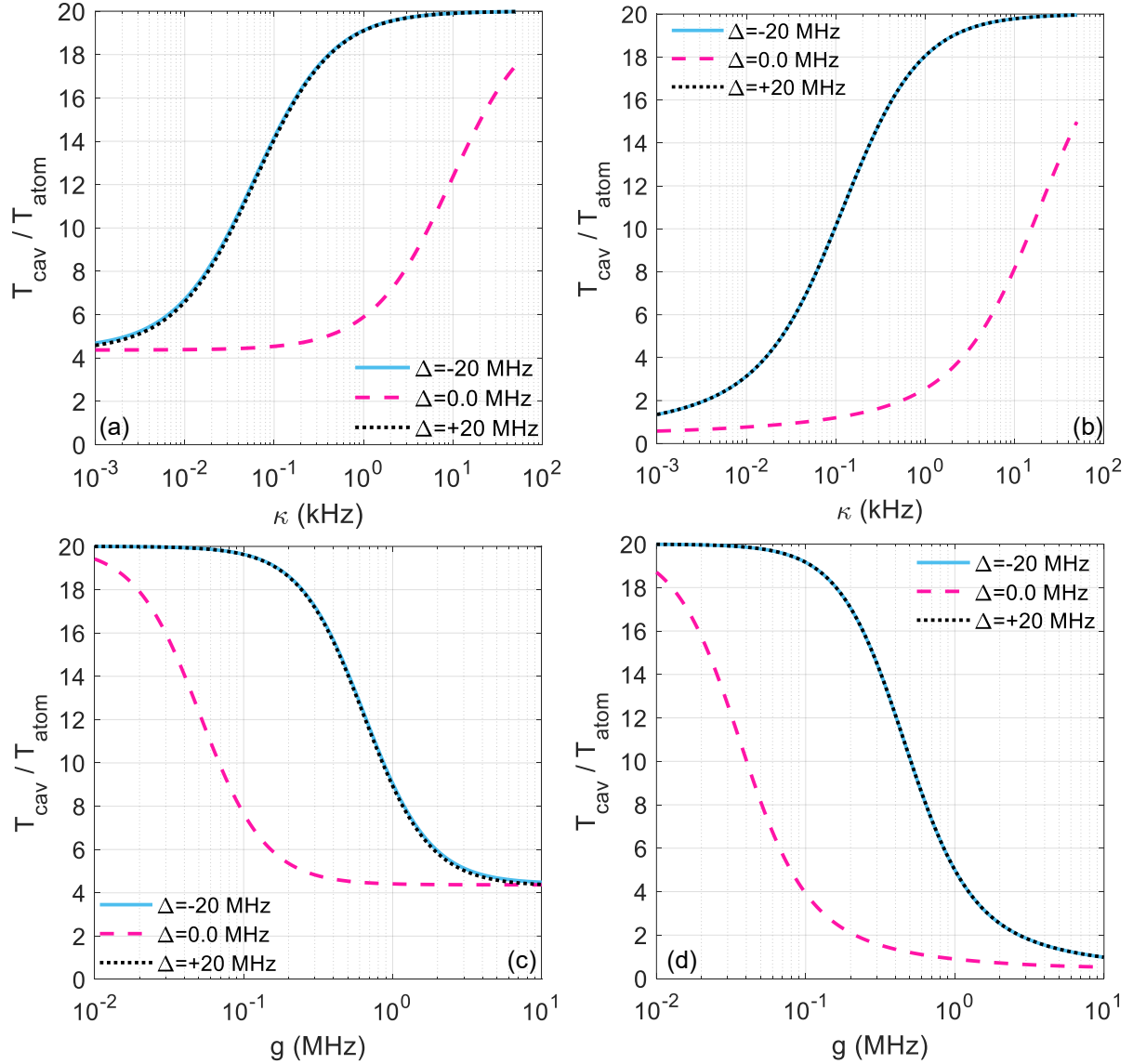
Figure 2: *(a,b) Dependence of cavity cooling on phonon coupling.* The steady-state temperature ratio $T_{\text{cav}}/T_{\text{atom}}$ is shown as a function of the cavity–phonon energy-damping rate κ for the one-atom (a) and two-atom (b) interaction models. In the weak-phonon-coupling regime, the correlated atomic stream dominates the energy balance and drives the cavity far from the environmental phonon bath. In the one-atom case (a), $T_{\text{cav}}/T_{\text{atom}}$ saturates near ~ 4 as $\kappa \to 0$, while in the two-atom case (b) the collective interaction enables genuine refrigeration, with $T_{\text{cav}}/T_{\text{atom}} \to 0.5$ in the same limit. As κ increases, the phonon bath increasingly overwhelms the stream-induced cooling and forces the cavity back toward its thermal equilibrium value $T_{\text{cav}} \to T_{\text{bath}}$. The crossover marks the departure from the idealized $\kappa = 0$ limit and quantifies the practical dissipation pathways present in superconducting microwave cavities. *(c,d) Dependence on cavity-atom coupling strength g.* Panels (c) and (d) show $T_{\text{cav}}/T_{\text{atom}}$ versus coupling g for the one-atom and two-atom models, respectively. Increasing g strengthens each weak collision $\phi = g\tau \ll 1$, amplifying the stream-induced Lindblad rates and thereby deepening the cavity cooling window. In both cases the curves saturate at the same limiting values observed in (a) and (b), near ~ 4 for the one-atom model and ~ 0.5 for the two-atom model, reflecting the intrinsic balance between excitation absorption and emission imposed by the correlated atomic reservoir. In the weak-coupling regime the stream cannot compete with phonon heating, while stronger g enables the engineered reservoir to impose its own nonequilibrium detailed balance on the cavity mode. These panels highlight an experimentally tunable transition between bath-dominated and reservoir-dominated cavity steady states.

15

In the one-atom model, Figure 2 (a) shows the dependence of $T_{\text{cav}}/T_{\text{atom}}$ on the cavity–phonon damping rate κ. For very small κ, the cavity scarcely exchanges energy with the phonons, and the correlated atomic stream fully dominates the energy balance. In this limit the cavity saturates at the intrinsic stream-imposed detailed balance, yielding $T_{\text{cav}}/T_{\text{atom}} \to 4$. This reproduces the behavior predicted in earlier idealized analyses that neglected external baths.[10] As κ increases, however, the phonon bath injects excitations that gradually overwhelm the weak-collision channel, forcing the cavity back toward the hotter environmental temperature. The smooth crossover in Figure 2 (a) therefore captures the realistic dissipation pathways present in superconducting microwave resonators, where phonon leakage cannot be ignored.

The two-atom model in Figure 2 (b) exhibits the same qualitative trend but with a dramatically different limiting behavior. When $\kappa \to 0$, the cavity is no longer driven toward a hotter steady state, but instead is cooled below the atom-pair temperature, reaching $T_{\text{cav}}/T_{\text{atom}} \to 0.5$. This quantum-enhanced refrigeration arises from the collective interaction of both atoms with the cavity, which modifies the upward-downward transition rates and allows the correlated pair to impose a colder effective detailed balance on the mode. As κ increases, phonon-induced excitations again dominate, eventually washing out the cooling advantage and restoring $T_{\text{cav}} \to T_{\text{bath}}$.

Panels (c) and (d) examine the complementary dependence on the cavity-atom coupling strength g. Increasing g enhances the per-collision rotation angle $\phi = g\tau$, amplifying the stream-induced Lindblad rates that govern the cooling dynamics. In the one-atom model (c), weak coupling leaves the cavity close to the phonon-dominated state, while stronger coupling drives it toward the saturated limit near $T_{\text{cav}}/T_{\text{atom}} \sim 4$. In the two-atom case (d), the same trend is observed, but the saturation occurs at the much colder value $T_{\text{cav}}/T_{\text{atom}} \sim 0.5$. Increasing g therefore extends the domain where the engineered reservoir dominates over the phonon bath and reveals the stronger cooling power of the collective two-atom interaction.

Taken together, Figure 2 (a–d) identifies the two essential experimental control knobs for nonequilibrium cavity refrigeration: (i) the suppression of unwanted phonon coupling (κ), and (ii) the enhancement of intentional atom-cavity interactions (g). Efficient cooling requires the engineered reservoir to dominate over environmental heating. This can be achieved either by operating with high cavity quality factors (small κ) or by increasing g so that the correlated atomic stream imposes its own detailed balance. The two-atom model demonstrates that collective correlations can significantly outperform the one-atom case, enabling the cavity temperature to be driven below the atomic reservoir temperature, an important capability for integrating such cavities with thermally sensitive quantum devices such as quantum dots, spin qubits, and bosonic memories.

3.3   Weak influence of pair correlations and global structure of the cooling landscape

Figure 3 (a–d) explores how intra-pair correlations and global parameter variations shape the steady-state temperature of a phonon-tethered cavity. Whereas detuning and phonon damping govern the dominant cooling-heating balance, the intra-pair exchange interaction λ modulates the internal structure of the correlated atomic reservoir and therefore affects the detailed balance imposed on the cavity. The effect, however, depends critically on whether one or both atoms interact with the cavity.

In the one-atom model, Figure 3 (a) shows that $T_{\text{cav}}/T_{\text{atom}}$ exhibits only a weak dependence on λ, and in fact increases slightly as λ grows. This behavior follows from the structure of the arrival coefficients in the one-subsystem configuration. Although the incoming thermal pair is described by the weights $\left(\rho_e, \rho_g, \rho_d, \rho_{nd}\right)$ of Eqs. (2)-(3), only one spin interacts with the cavity, so the effective upward and downward weights reduce $r_1 = \rho_e + \rho_d$ and $r_2 = \rho_g + \rho_d$. The coherence term ρ_{nd}, responsible for the correlated advantages in the two-atom case, drops out entirely. Consequently, the cooling-relevant difference $r_2 - r_1 = \rho_g - \rho_e$ depends only on the single-spin splitting ω and is independent of λ except for normalization via the partition function Z. Increasing λ increases the weight of the ρ_d manifold, which appears symmetrically in both r_1 and r_2. The net effect is a mild reduction in stream-induced cooling efficiency, hence the slow rise of $T_{\text{cav}}/T_{\text{atom}}$ with increasing λ.

The situation is qualitatively different in the two-atom model, where both atoms interact simultaneously with the cavity. In this case (Figure 3 (b)), the stream-induced rates depend on the full set of two-subsystem

coefficients $r_1^{(2)}, r_2^{(2)}$, which now contain the pair coherence ρ_{nd}. Increasing λ enhances the coherent mixing between $|eg\rangle$ and $|ge\rangle$, strengthening the collective interaction channel and suppressing the net upward transition rate relative to the downward one. The result is a monotonic decrease of T_{cav}/T_{atom} with increasing λ, signaling a genuine quantum-enhanced refrigeration mechanism unavailable in the one-subsystem configuration.
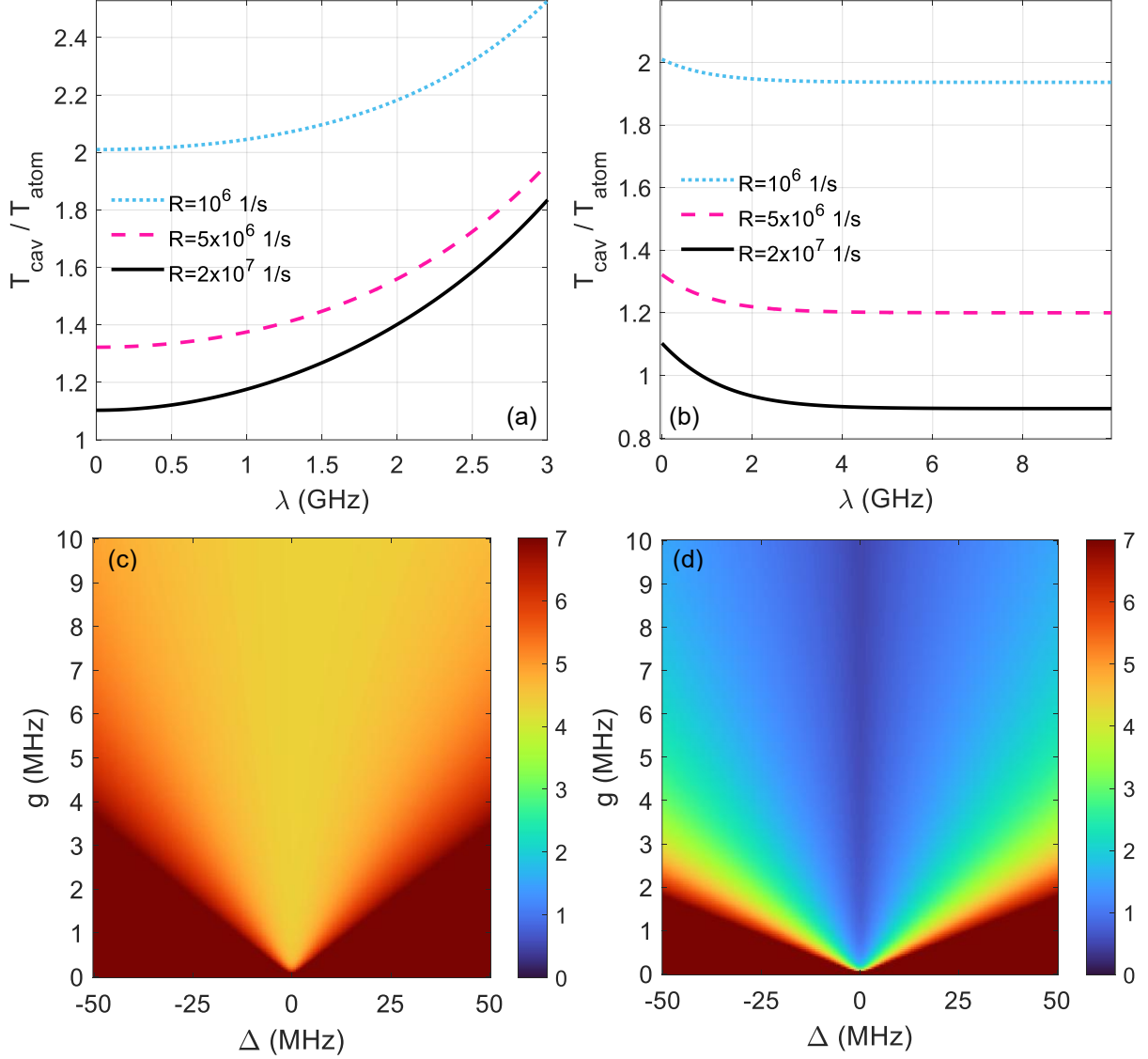

Figure 3: *(a,b) Influence of the intra-pair exchange coupling λ on cavity cooling.* The ratio T_{cav}/T_{atom} is plotted as a function of the exchange coupling λ for the one-atom (a) and two-atom (b) interaction models. The exchange term λ reshapes the correlated pair's internal populations $(\rho_e, \rho_g, \rho_d, \rho_{nd})$ and thereby modifies the stream-imposed detailed balance acting on the cavity. In the one-atom model (a), increasing λ raises T_{cav}/T_{atom}, reflecting the reduced ability of the correlated pair to extract entropy when only a single subsystem interacts with the cavity. In contrast, in the two-atom model (b), stronger exchange enhances collective coherence and improves the net cooling power, leading to a monotonic decrease of T_{cav}/T_{atom} with λ. *(c,d) Two-dimensional cooling landscape versus detuning and coupling strength.* Panels (c) and (d) show color maps of T_{cav}/T_{atom} as a function of both the detuning Δ and the atom-cavity coupling strength g, for the one-atom and two-atom models, respectively. Cooling "valleys" appear near resonance and deepen with increasing g, while off-resonant or weak-coupling regions are dominated by phonon-induced heating. The two-atom model (d) exhibits a markedly stronger refrigeration effect and a broad

region where $T_{\text{cav}}/T_{\text{atom}} < 1$, indicating true cavity cooling below the atom-stream temperature. These maps delineate the operational regime in which correlated atomic pairs can overcome phonon heating and impose a colder nonequilibrium steady state on the cavity.

Figure 3 (c) and (d) present two-dimensional maps of $T_{\text{cav}}/T_{\text{atom}}$ as functions of detuning Δ and coupling strength g. These maps synthesize, in a single representation, the competing influences of spectral overlap and interaction strength. Near resonance, spectral matching is optimal and increasing g amplifies each weak collision, producing the "cooling valleys" characteristic of effective stream-dominated refrigeration. Far from resonance, the Lorentzian overlap $L(\Delta)$ suppresses stream-induced exchange, and phonon-induced heating drives the cavity toward T_{bath}, generating broad heating plateaus at large $|\Delta|$.

The contrast between Figure 3 (c) and (d) reinforces the fundamental distinction between the one-atom and two-atom models: correlations play only a minor role when one subsystem interacts with the cavity, but become central when both atoms couple collectively. In the two-atom landscape, the enhanced coherence channels produce a wide region where $T_{\text{cav}}/T_{\text{atom}} < 1$, highlighting a robust refrigeration regime not accessible to the one-subsystem.

3.4 The effect of phonon damping

Figure 4 directly illustrates how cavity-phonon dissipation reshapes the steady-state temperature in both the one-atom and two-atom interaction models. When the cavity-phonon damping rate $\kappa \to 0$, the cavity becomes effectively isolated from its environmental phonon bath, and its temperature is governed almost entirely by the correlated atomic reservoir. In this limit the one-atom model saturates at the characteristic value $T_{\text{cav}}/T_{\text{atom}} \sim 4$, while the two-atom model reaches the substantially colder value $T_{\text{cav}}/T_{\text{atom}} \sim 0.5$. These limiting ratios reproduce the predictions of the idealized $\kappa = 0$ theory and serve as reference baselines for evaluating all realistic scenarios.[10]
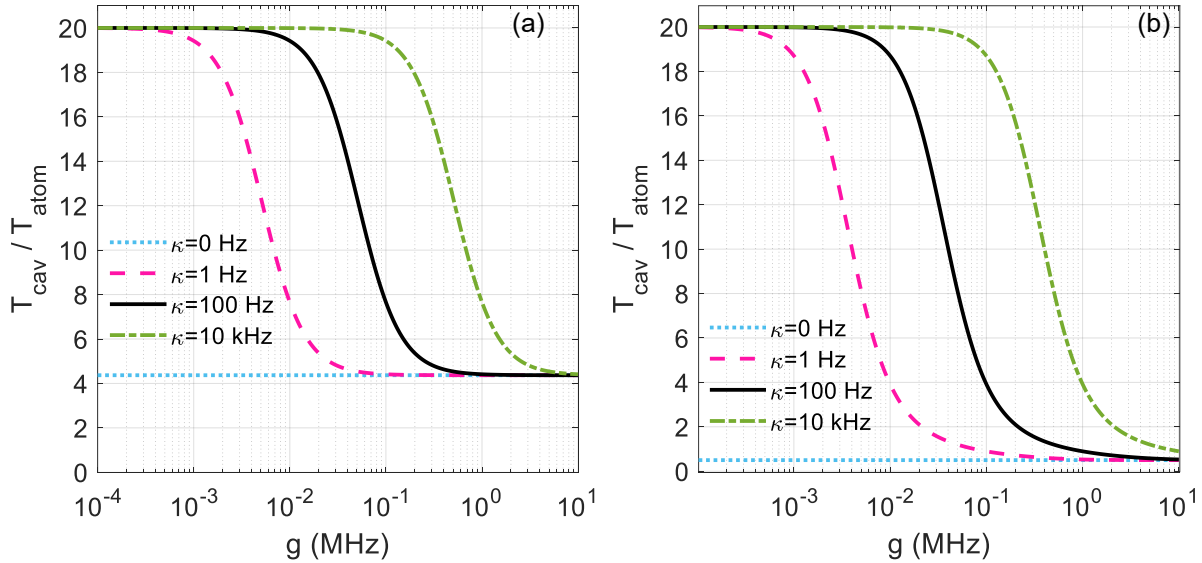

Figure 4: *Influence of cavity–phonon damping on cavity cooling.* The ratio $T_{\text{cav}}/T_{\text{atom}}$ is plotted for several cavity-phonon damping rates κ in the one-atom (a) and two-atom (b) interaction models. These curves illustrate the crossover between the idealized limit $\kappa \to 0$, where the cavity is effectively isolated from its phonon environment, and the realistic phonon-tethered regime relevant for superconducting microwave cavities. In the weak-phonon-coupling limit, the cavity decouples from the environmental bath and the steady state is governed almost entirely by the correlated atomic reservoir. In this regime the one-atom model saturates near $T_{\text{cav}}/T_{\text{atom}} \sim 4$, whereas the collective two-atom model reaches significantly colder values $T_{\text{cav}}/T_{\text{atom}} \sim 0.5$, reflecting its enhanced refrigeration capability. As the damping rate κ increases, phonon-induced excitations progressively suppress the stream's ability to extract entropy, and the cavity relaxes toward the phonon-bath temperature T_{bath}. The sensitivity of these curves to κ demonstrates how even modest phonon leakage reshapes the cooling window and establishes practical limits on stream-dominated refrigeration in realistic superconducting cavity platforms.

As soon as κ becomes nonzero, even at values as small as a few hertz, phonon-induced excitations begin to compete with the entropy extraction performed by the atomic stream. This additional thermalization pathway progressively pulls the cavity toward the phonon-bath temperature T_{bath}, weakening the stream-imposed detailed balance. The resulting crossover is clearly visible in both panels of Figure 4: for increasing κ, the cavity temperature rises from its stream-dominated value toward the phonon-dominated equilibrium. Because the one-atom model begins from a relatively hot baseline, its temperature rises more rapidly, whereas the two-atom model retains its refrigeration advantage over a broader window of phonon damping.

These trends delineate the practical regime in which engineered reservoir cooling can outperform environmental dissipation. Even modest phonon damping significantly narrows the operational window for strong cooling, emphasizing the importance of high-quality superconducting cavities for realizing stream-driven refrigeration. At the same time, the two-atom model demonstrates a substantially greater robustness to phonon leakage, reflecting the enhanced cooling power generated by pair coherence and collective interaction.

Thus, Figure 4 confirms both the consistency of our model with the $\kappa \to 0$ limit and the necessity of incorporating phonon coupling when assessing cooling performance in realistic experimental platforms.

A noteworthy distinction between the one-atom and two-atom coupling models becomes evident when examining the detuning dependence in the idealized limit of vanishing cavity-phonon contact ($\kappa \to 0$), as shown in Figure 5. In the one-atom configuration, the ratio $T_{\mathrm{cav}}/T_{\mathrm{atom}}$ displays a weak but discernible asymmetry as the atomic transition $\omega = \omega_1 + \Delta$ is swept over the range $\Delta \in [-50,50]$ MHz. This asymmetry arises from the unequal thermal weights $\rho_e \propto e^{-\beta\hbar\omega}$ and $\rho_g \propto e^{+\beta\hbar\omega}$, which feed directly into the detailed balance through the one-subsystem arrival coefficients r_1 and r_2. Because only a single spin interacts with the cavity, these coefficients retain the antisymmetric dependence on Δ, leading to a slow monotonic drift of $T_{\mathrm{cav}}/T_{\mathrm{atom}}$ as the atomic frequency is tuned.
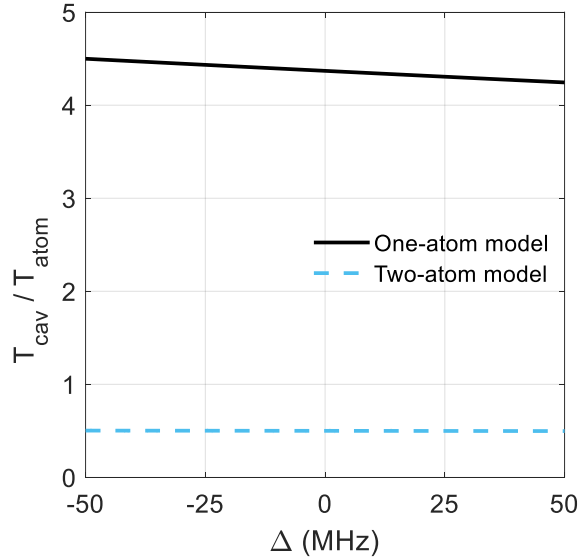

Figure 5: *Effective cavity temperature in the one- and two-atom interaction models in the absence of phonon coupling.* The ratio $T_{\mathrm{cav}}/T_{\mathrm{atom}}$ is shown as a function of the detuning $\Delta = \omega - \omega_1$ for $\kappa = 0$, isolating the intrinsic effect of the correlated atomic reservoir. In the one-atom model, the curve exhibits a weak asymmetry as Δ is swept over ±50 MHz: $T_{\mathrm{cav}}/T_{\mathrm{atom}}$ decreases approximately linearly with increasing detuning and continues to fall even for $\Delta > 0$. This slight asymmetry originates from the unequal thermal weights ρ_e and ρ_g that determine the effective upward and downward transition rates when only a single atom couples to the cavity. The two-atom model displays a much weaker dependence on Δ. Because both atoms interact collectively with the cavity, the relevant upward–downward rates incorporate symmetric pair-coherent contributions that suppress the detuning-induced imbalance present in the one-atom configuration. As a result, the two-atom curve is nearly symmetric about $\Delta = 0$, reflecting the enhanced robustness of collective cooling against detuning.

In contrast, when both atoms interact with the cavity, the correlated contributions from the single-excitation manifold, encoded in ρ_d and, crucially, the coherence term ρ_{nd}, modify the effective upward and downward transition rates. These collective terms suppress the antisymmetric Δ-dependence present in the one-atom case, producing an almost symmetric and significantly weaker detuning dependence. The two-atom model thereby exhibits a nearly flat response across the same detuning range.

This contrast highlights the deeper role played by pair correlations: even in the absence of any phonon bath, collective coupling alters the effective reservoir seen by the cavity, smoothing out detuning asymmetries that are otherwise unavoidable in single-spin interaction models.

4. Experimental Mapping to a cQED Architecture

4.1 Motivation and Cryogenic Context

A central challenge in scaling quantum hardware arises from the steep drop in available cooling power as one descends below the kelvin scale in standard dilution refrigerators. While the 20 mK stage typically offers only on the order of 10-20 µW, the 100 mK stage reaches sub-milliwatt levels ($\approx$ 0.5 mW in modern systems), illustrating a multi-order-of-magnitude disparity across the cryostat tiers; representative specifications from commercial systems document $\approx$ 16 µW at 20 mK and $\approx$ 0.5 mW at 100 mK for LD-class units.[1] By contrast, auxiliary 1 K stages and dedicated 1 K systems can supply far larger cooling capacities, often at or above the $\gtrsim$ 100 mW scale, making the 1-4 K envelope an attractive "high-power zone" for co-locating electronics, filtering, and other infrastructure.[2]

This imbalance forces nearly all quantum devices (superconducting qubits and resonators, semiconductor spin qubits, low-noise amplifiers, and sensitive readout circuitry) to reside at the lowest-temperature plate, where cooling resources are scarcest and wiring heat loads become the dominant architectural constraint. Reviews of superconducting-qubit hardware emphasize these system-level pressures and the importance of cryogenic staging and thermal budgeting.[8]

A promising direction for alleviating this bottleneck is to relocate as much classical and passive hardware as possible to higher-temperature stages (1-4 K) while employing engineered quantum reservoirs to pull specific degrees of freedom, selected cavity modes, qubits, or mesoscopic devices, to effective temperatures far below the ambient of the supporting stage. The broader idea is rooted in quantum thermodynamics: few-qubit thermal machines and autonomous quantum absorption refrigerators can impose a desired detailed balance on a target mode without net external work, functioning as compact quantum coolers that create local regions of low entropy even inside a comparatively warm environment.[15,16] In parallel, rapid progress in cryo-CMOS electronics at the 4 K tier is validating the complementary system design strategy of shifting classical control and readout overhead to warmer plates, thereby reserving the coldest stage primarily for components that genuinely require millikelvin operation.[40,41]

Within this context, the two-atom (two-qubit) refrigerator architecture explored here functions as an engineered reservoir that can operate at a warmer stage yet impose a colder effective temperature on a target cavity mode or device degree of freedom. By combining the abundant cooling power available around 1 K with an autonomous quantum-refrigeration mechanism, this approach aims to relieve thermal budgets at the base plate while still preserving the low-entropy conditions required locally for high-fidelity operation.[3,11]

Figure 6 summarizes the circuit-QED implementation of the two-qubit refrigerator within a cryogenic environment. A high-Q 3D cavity, hosting the refrigerated mode at effective temperature T_{cav}, is embedded in a phonon bath at T_{bath} and coupled coherently to a pair of superconducting qubits that constitute the engineered atomic reservoir at T_{atom}. The schematic highlights the coherent Jaynes–Cummings exchange between the qubits and the cavity, the dissipative reset channel that returns the qubit reservoir to a low-entropy state via a Purcell-filtered decay path, and the resulting closed heat-flow loop in which entropy is repeatedly pumped from the cavity into the engineered reservoir and then into the 1 K stage. This layout makes explicit how a locally cold cavity mode can be sustained inside a comparatively warm but high-power cryogenic tier, setting the stage for the quantitative temperature profiles presented in Figure 7.
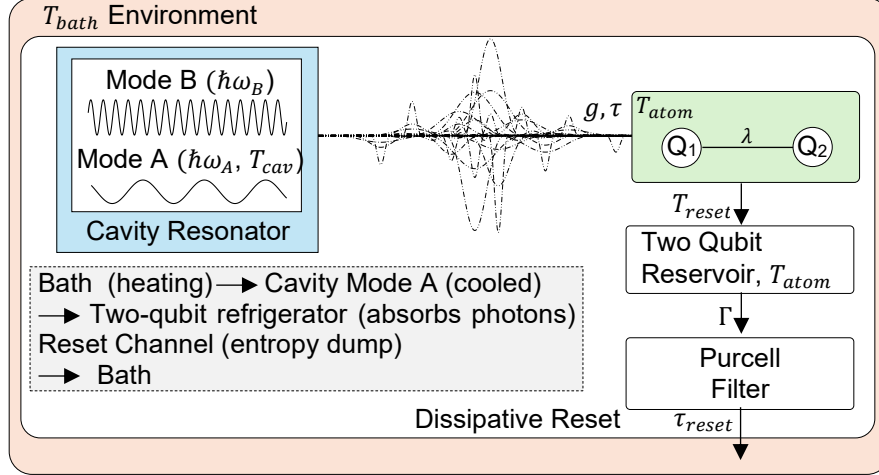
Figure 6: Circuit-QED implementation of the two-qubit refrigerator inside a cryogenic environment. A high-Q 3D cavity hosting Modes A at an effective temperature T_{cav} is embedded in a phonon bath at T_{bath} and coupled via Jaynes-Cummings interactions g to a pair of superconducting qubits that constitute the engineered atomic reservoir at T_{atom}. The arrow labeled Γ represent dissipative channel from the qubits into a coarse-grained two-qubit reservoir, which is reset through a Purcell-filtered decay path at rate τ_{reset} into the T_{bath} stage. Together these processes realize a repeated-interaction refrigeration cycle that pumps entropy from the cavity into the engineered reservoir and ultimately into the bath, allowing the cavity mode A to equilibrate at T_{cav} while residing on the same high-power cryogenic tier.

Figure 7 illustrates the practical significance of the engineered reservoir by showing the steady-state cavity temperature as a function of the cavity–bath damping rate κ for several bath temperatures spanning the full cryogenic range relevant to superconducting hardware. In the one-subsystem case [Figure 7 (a)], the engineered reservoir drives the cavity to an effective temperature of $T_{\text{cav}} \approx 219$ mK in the limit of negligible bath contact, independently of T_{bath}. Increasing κ couples the mode more strongly to the environment, gradually pulling the cavity toward T_{bath}: for a 100 mK bath the engineered refrigeration cools toward the bath temperature, while for higher bath temperatures (500 mK, 1 K, 4 K) the cavity instead warms toward the ambient. By contrast, the two-subsystem configuration [Figure 7 (b)] exhibits far stronger refrigeration: in the idealized limit $\kappa \to 0$, the cavity approaches $T_{\text{cav}} \approx 25$ mK, irrespective of the bath temperature. This demonstrates that pair quantum correlations enable the engineered reservoir to impose a substantially colder detailed balance on the cavity mode. In realistic devices, where κ can be engineered to lie well below the kilohertz scale through careful cavity design and shielding, these results suggest that sub–100-mK effective cavity temperatures are achievable, even when the surrounding cryostat is at 1 K or higher. This establishes the feasibility of using a two-qubit refrigerator to create localized millikelvin regions inside high-power cryogenic stages, enabling cold microwave modes for quantum memories or as refrigeration interfaces for semiconductor qubits.

A practical reason to employ a two-atom (two-qubit) working medium is that direct "algorithmic" cooling of a bosonic cavity mode is fundamentally resource-intensive. A cavity has an infinite ladder of Fock states; cooling it algorithmically would require removing excitations at arbitrarily high photon numbers or equivalently engineering a highly selective dissipative channel that enforces detailed balance at a temperature below the ambient stage. Few-level systems, by contrast, admit fast, repeatable resets. In superconducting cQED, qubits can be reinitialized either autonomously by engineered dissipation or actively by measurement-based feedback, with mature experimental implementations. Fast unconditional all-microwave qubit reset and deterministic measurement-feedback reset have been demonstrated with sub-microsecond latencies, and driven-dissipative schemes autonomously stabilize target states, providing a compact route to entropy dumping.[7,8,9] These capabilities make qubits efficient *sacrificial refrigerants*, whereas the cavity serves as the cold stage that is repeatedly cooled through engineered contact with the qubit reservoir.
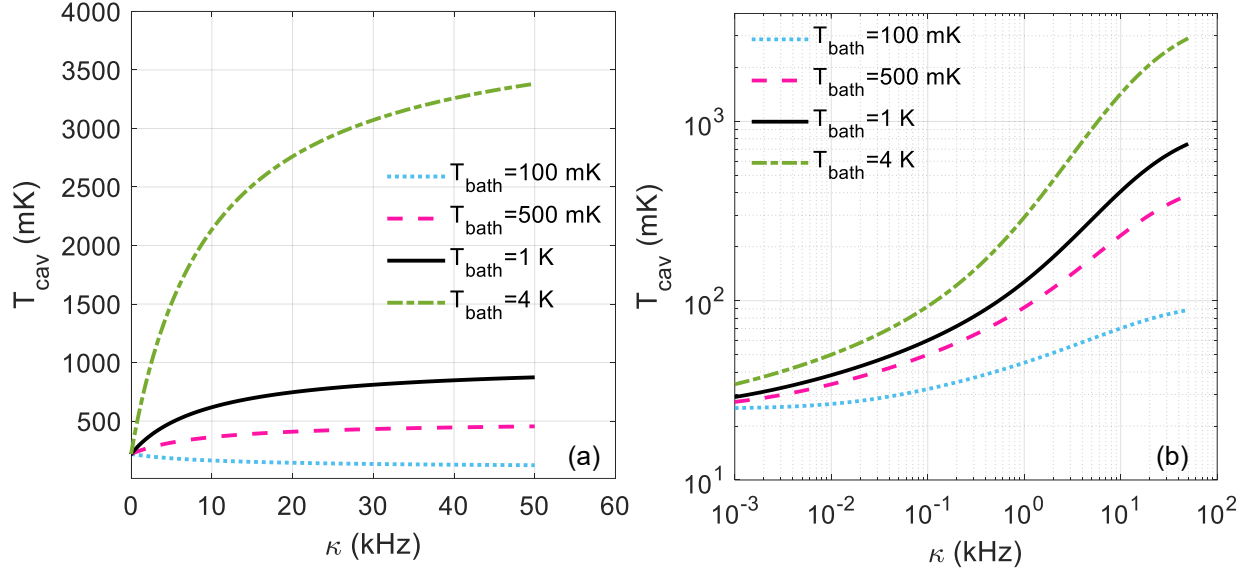
Figure 7: Steady-state cavity temperature T_{cav} versus cavity–bath damping rate κ for (a) one-subsystem coupling (only one atom interacts with the cavity) and (b) two-subsystem coupling (both atoms interact). Curves are shown for four ambient bath temperatures $T_{bath} = $ 100 mK, 500 mK, 1 K, 4 K. In (a), the one-atom configuration yields a minimum achievable cavity temperature of approximately $T_{cav} \approx$ 219 mK at $\kappa = 0$, independent of T_{bath}. As κ increases, the cavity gradually equilibrates with the bath: at $T_{bath} = $ 100 mK, the cavity cools toward 100 mK, while for higher T_{bath} it warms toward the bath temperature. In (b), the two-atom configuration enables significantly stronger refrigeration: for vanishing κ, the cavity reaches $T_{cav} \approx 25$ mK across all bath temperatures. Increasing κ again drives the steady state toward T_{bath}.

Using two qubits rather than one adds capabilities essential to our refrigerator. First, correlations in a two-qubit pair, embedded, for instance, in the singlet/triplet superpositions $|eg\rangle \pm |ge\rangle$, modify the upward and downward transition rates felt by the cavity. In the collision-model language, the coefficients (r_1, r_2) or their two-subsystem extensions $(r_1^{(2)}, r_2^{(2)})$ are shifted by pair coherence, altering the effective detailed balance and enabling quantum-enhanced cooling, where the cavity's temperature T_{cav} drops below the effective temperature of the pair. This mechanism parallels collective emission and absorption in correlated emitters (Dicke super- and subradiance) and is closely related to micromaser-style cavity pumping by successive ancillae.[14,42,43]

Second, a two-qubit working medium broadens the design space for engineered reservoirs. By preparing and resetting appropriate two-qubit manifolds, one can tailor an effective temperature, spectral response, and energy-exchange directionality with the cavity, central objectives in quantum reservoir engineering and autonomous refrigeration.[17,44,45]

Finally, this mapping is directly compatible with modern hardware: the two-atom system can be realized with two transmons (planar or 3D), or with flux/fluxonium-type qubits, all within the standard circuit-QED toolset. Strong and even ultrastrong light-matter couplings are routine, and tunable couplers provide wide, fast control of the qubit-qubit exchange needed to prepare and reset correlated states.[9,20,21,22] This establishes a clear experimental path for implementing the theoretical refrigerator analyzed in this work.

4.2 Realization with Two Superconducting Qubits and a 3D Cavity

The core elements of the proposed refrigerator, a high-Q microwave cavity and a pair of superconducting qubits, map naturally onto standard cQED hardware. A 3D superconducting cavity provides long photon lifetimes, clean electromagnetic mode structure, and compatibility with tunable and fixed-frequency qubits. In this architecture, the cavity plays the role of the cold working medium, while the two qubits act as a resettable quantum reservoir that repeatedly absorbs entropy from the cavity and dumps it into a cold load through active reset.

Each cooling cycle begins with preparing the two qubits in a prescribed mixed state with well-defined populations and pair coherence ($\rho_e, \rho_g, \rho_d, \rho_{nd}$). This can be achieved with a short sequence of single-qubit rotations and an entangling gate, optionally combined with engineered dissipation to stabilize the desired manifold. Such driven-dissipative state-preparation schemes are standard in quantum reservoir engineering, which uses the competition between coherent drive and controlled dissipation to autonomously stabilize target subspaces or entangled states.[23,24,25]

These preparation procedures realize the "initial ancilla state" assumed in the collision-model section of our theory. The coarse-grained Lindbladian emerging from repeated ancilla-cavity collisions is rigorously justified in the open-quantum-systems literature,[12] providing the microscopic basis for describing each engineered two-qubit pair as a single "collision" imparting an $\mathcal{O}(\phi^2)$ kick to the cavity, where $\phi = g\tau$ is the Jaynes-Cummings interaction angle.

To implement the interaction time τ assumed in the theory, the qubits are tuned into (near) resonance with the cavity for the desired interval by applying nanosecond-scale flux pulses. Experimental demonstrations across both 3D and planar cQED platforms show that qubit transition frequencies can be shifted by hundreds of MHz with sub–100-ns latencies, enabling rapid "engage" and "disengage" operations.[46,47] Tunable-coupler architectures and flux-tunable transmons routinely provide multi-hundred-MHz to multi-GHz frequency agility, allowing precise control of both the qubit-cavity detuning Δ and the inter-qubit exchange coupling λ.

During the engaged interval τ, the two-qubit system and the cavity undergo a weak Jaynes-Cummings exchange. By choosing $\phi = g\tau \ll 1$, a single interaction reproduces the weak-collision limit required in the theoretical model, including the detuning-filtered energy exchange rate governed by the Lorentzian overlap $L(\Delta)$. Experimental control of detuning is routine in cQED, with MHz- to GHz-scale offsets readily programmed by flux modulation.

After interaction with the cavity, both qubits must be returned rapidly to a low-entropy state before the next cycle. Reset is the thermodynamic "work step" that evacuates the entropy absorbed from the cavity. Circuit-QED experiments now support several mature reset modalities, all compatible with MHz-rate refrigeration cycles:

1. Dissipative (Purcell-enhanced) reset:
   The qubit is temporarily coupled to a low-Q mode or Purcell-filtered decay channel, enabling unconditional relaxation with time constants of order 10^2 ns and residual excitations at or below $10^{-3} - 10^{-2}$.[26,27,28,29]
2. Measurement-and-feedback reset:
   High-fidelity projective measurement followed by a conditional π-pulse yields near-ground-state preparation on microsecond timescales and with high robustness[24,48]
3. Autonomous (driven-dissipative) reset:
   Parametric or multi-tone microwave drives engineer an attractor in the qubit's state space, enabling unconditional ground-state reset in sub–500-ns without classical feedback.[23,32,33]
4. Stimulated-emission and parametric-sideband reset:
   Recently demonstrated architectures use broadband or parametrically driven couplings to funnel qubit excitations into a cold bath with sub–100-ns latencies while suppressing unwanted Purcell decay during idle periods.[22,31]

These reset modalities have been extensively optimized in the cQED community and reliably maintain effective qubit temperatures in the 30-80 mK range at 5-7 GHz transition frequencies, consistent with residual populations of ~1-3%. Because the 1-K stage provides abundant cooling power, the classical microwave resources needed to drive, measure, and reset the qubits are easily supported at that temperature.

Once preparation, interaction, and reset are available, the full repeated-interaction refrigerator is straightforward to realize. Each "cooling cycle" consists of:

1. Prepare correlated two-qubit state.
2. Bring both qubits into resonance with the cavity for time τ.
3. Allow an $\mathcal{O}(\phi^2)$ energy exchange event with adjustable detuning Δ.

4. Disengage and reset both qubits.
5. Repeat at a programmable rate R.

Randomizing the start time of each cycle (or using an aperiodic digital trigger) reproduces the Poissonian arrival statistics underlying the collision model and the master equation used in sections 1 and 2. This mapping has deep roots in the micromaser literature, where successive atoms passing through a cavity generate an effective Lindblad generator with upward and downward rates proportional to $Rr_1\phi^2$ and $Rr_2\phi^2$.[14] Under realistic parameters (MHz-class arrival rates, small angles $\phi \lesssim 0.1$, detunings in the 10-100-MHz range, and cavity damping 10-100 kHz) the resulting effective damping $\Gamma_\downarrow$ and source term $J_\uparrow$ yield cavity-cooling time constants of order 10-100 μs, compatible with standard cQED coherence windows.

Thus, the repeated-interaction refrigerator studied in our theory can be implemented almost directly using off-the-shelf cQED components. All required ingredients (fast state preparation, rapid tunability, high-fidelity reset, and multimode cavity engineering) are already experimentally demonstrated, establishing the feasibility of recreating our idealized two-atom model within present-day superconducting-qubit hardware.

4.3 Reset Mechanisms and Achievable Temperatures

Reset plays a central role in enabling the two-qubit refrigerator, as it constitutes the entropy-dumping step required to maintain the working medium at low effective temperature. Without a fast and high-fidelity return to a low-entropy state, the qubits would accumulate excitations extracted from the cavity and the refrigeration cycle would saturate. Within circuit QED, qubit reset has matured into a well-developed technological capability, with several experimentally established modalities that operate at rates compatible with the MHz-class repeated-interaction cycles assumed in our theoretical model. These reset channels exploit either engineered dissipation or active measurement and control to funnel population out of the excited state and thereby maintain the qubit subsystem at a low effective temperature.

Dissipative reset is often realized through Purcell-enhanced relaxation, where the qubit is temporarily coupled to a low-Q auxiliary mode or a dedicated Purcell filter so that the excited state decays rapidly into a cold load. Experiments have demonstrated unconditional ground-state reset with characteristic time constants on the order of 10^2 ns and with residual excited-state populations as low as $10^{-3} - 10^{-2}$; more recent architectures employ tunable or multi-mode Purcell filters to combine rapid reset with protection against unwanted decay during coherent operations.[21,22,26,29] A complementary approach uses measurement followed by classical feedback, wherein a high-fidelity projective measurement is performed and an appropriate conditional π-pulse is applied to return the qubit to its ground state. Deterministic, measurement-based reset routinely achieves near-ground-state preparation within microsecond time intervals and has enabled repeated initialization well beyond the limits set by intrinsic T_1 relaxation.[24,48]

Autonomous, measurement-free reset provides yet another path to rapid entropy removal. In such schemes, the competition between coherent microwave drive and engineered dissipation creates an attractor in the qubit state space that deterministically funnels population toward the ground state, eliminating the need for feedback loops. Driven-dissipative protocols have prepared fixed-frequency transmons to their ground state within sub–500-ns windows and have been extended to the unconditional stabilization of entangled two-qubit states, making the approach particularly appealing for thermal machines based on correlated qubit pairs.[23,32,33] Related ideas activate stimulated emission or parametric sideband transitions to accelerate population transfer into a lossy bath. Architectures employing broadband waveguides or parametrically modulated couplers have reported unconditional reset latencies below 100 ns, together with the ability to suppress Purcell decay during idle times through tunable coupling elements.[22,27]

These reset modalities are powerful enough to maintain the two-qubit subsystem at an effective temperature in the 30-80 mK range even while operating at a 1 K cryostat stage. A residual excited-state probability of only a few percent at qubit transition frequencies in the 5-7 GHz range corresponds directly to effective temperatures of this order, consistent with the targets needed for the refrigerator. The classical microwave resources required to implement these resets (high-power drives, broadband control lines, and fast measurement electronics) can be supported readily at the 1 K tier, which typically offers cooling powers in the hundreds of milliwatts. Commercial 1 K platforms provide between 200-700 mW at temperatures around 1-1.2 K, and dedicated 1 K-loop stages integrated into dilution refrigerators offer similarly high

capacities.[1,5] These conditions make the 1 K environment particularly attractive for hosting the qubit-reservoir infrastructure, with the cavity mode acting as the object to be cooled inside this warm but powerful stage.

The resulting steady-state temperatures predicted by our collision-model dynamics reflect this balance. Under realistic conditions (MHz-scale repetition rates, small interaction angles $\phi = g\tau$, weak cavity-bath coupling κ in the 10-100 Hz to 1 kHz range, and detuning-controlled exchange governed by the spectral filter $L(\Delta)$) the cavity cools toward a steady state set predominately by the engineered qubit reservoir rather than by the ambient 1 K bath. The resulting cavity temperature T_{cav} lies in the 50-120 mK range across broad regions of parameter space, and the effective cooling time constants fall in the $10\text{-}100\,\mu s$ band, consistent with the $\mathcal{O}(R\phi^2)$scaling of repeated-interaction refrigerators and with the coherence times accessible in high-Q 3D cavities.

The multimode nature of 3D cavities further expands the utility of these reset mechanisms. When a second cavity mode (Mode B) is used as a memory or as an interface to a semiconductor quantum dot, it can be cooled opportunistically, only when it stores no quantum information, by temporarily activating a parametric beam-splitter interaction $g_{AB}(t)$ that swaps excitations with the refrigerated Mode A. Recent demonstrations of high-isolation, high-fidelity parametric mode converters, including SNAIL-based and parity-protected devices, confirm that such inter-cavity beam-splitters can be activated with large on-off ratios and low added loss.[37,38] In this "cool-before-load" protocol, entropy flows from Mode B into Mode A and then into the engineered two-qubit reservoir through the reset channel, leaving Mode B cold and ready to store quantum information or couple to an external device.

Direct algorithmic cooling of a harmonic oscillator, by contrast, remains fundamentally difficult. Because of the cavity's infinite-dimensional Hilbert space, removing population from arbitrarily high Fock states would require non-Gaussian, number-resolved operations or photon-number-specific measurements that are experimentally demanding even in strongly dispersive cQED architectures. The literature on heat-bath algorithmic cooling (HBAC) targets finite-dimensional registers and consistently relies on rapidly resettable ancilla qubits as the fundamental resource for entropy compression.[12,47] General constraints on Gaussian thermal operations in bosonic systems reinforce this limitation, as achieving very low effective temperatures requires either non-Gaussian resources or auxiliary systems that can be efficiently reset, returning us to the two-qubit reservoir as the minimal realistic module for cooling a cavity mode.[30,47,49,53,54]

Taken together, these developments establish that the two superconducting qubits used in our refrigerator can reliably be reset to effective temperatures in the tens of millikelvin range at rates exceeding those required for the repeated-interaction dynamics. They therefore provide exactly the type of low-entropy, rapidly recyclable ancilla needed for enforcing a cold detailed balance on a cavity mode situated within a high-power 1 K environment.

5. Outlook

The experimental analogue of the theoretical "two-atom refrigerator" is a pair of actively reset superconducting qubits that repeatedly interact with a high-Q 3D microwave cavity mode. In this picture the qubits function as a sacrificial, low-entropy reservoir maintained far below the ambient cryostat temperature by fast dissipative or measurement-based resets; their repeated, weak, and detuned-tunable collisions impose an effective detailed balance on the cavity, cooling it to tens of millikelvin even when the cryostat itself operates near 1 K. This is precisely the regime in which 1 K platforms provide abundant cooling power, hundreds of milliwatts to the watt class, so the entropy removal required for frequent qubit resets can be supplied without stressing the base-plate budget, while the cavity experiences a tailored quantum reservoir rather than the warm phonon bath. The repeated-interaction framework gives a microscopically controlled route from discrete ancilla shots to a Lindbladian for the cavity, with the micromaser literature and modern collision-model theory offering both the conceptual and quantitative underpinnings for this mapping.[14,6]

Near-term milestones are within reach. Fast, high-fidelity qubit resets at the 10^2-ns scale, via Purcell-enhanced dissipation, parametric channels, or autonomous reservoir engineering, are now routine, and autonomous entanglement stabilization of two-qubit manifolds has been demonstrated in cavity- and

waveguide-based settings. In our architecture these elements provide the "reset and reprepare" primitive that clamps the ancilla pair to a prescribed mixed state with controllable correlations, which in turn fixes the upward/downward coefficients in the collision map and therefore the cavity's steady-state temperature. Experimentally, one can validate the cooling by cavity thermometry (e.g., sideband spectroscopy on a weak probe qubit or mode) and by measuring the ancilla energy flow during cycles; both readouts are compatible with MHz repetition and small-angle exchanges.[32,46]

Once established, a precooled cavity enables device-level payoffs. Gate-defined semiconductor double quantum dots (DQDs)[50] have reached strong coupling with microwave cavities in III-V and Si/SiGe platforms; in such devices a colder cavity directly suppresses thermal photon occupation at the qubit transition and reduces phonon-assisted leakage to unwanted orbitals, improving spin-qubit initialization and charge-noise resilience at elevated cryostat temperatures. A second, complementary pathway is inter-cavity refrigeration: designate one cavity mode as the refrigeration interface and use a programmable beam-splitter to swap entropy from a memory or DQD-coupling mode when it is empty ("cool-before-load"), a control primitive already standard in bosonic-code experiments. Together these uses make the refrigerated cavity a versatile low-entropy resource embedded in a warm 1 K environment.[35,36,39]

From a systems perspective, the architecture addresses a central scalability bottleneck: millikelvin stages offer only tens of microwatts at the mixing chamber, whereas 1 K stages can sustain two to three orders of magnitude more power for control electronics, pumps, and fast flux drives. Relocating control to 1 K while generating local sub–100-mK pockets via qubit-engineered reservoirs provides a realistic path toward larger channel counts without saturating the base plate. Theoretical control is aided by the detuning-aware collision model: the same small-angle interaction can be spectrally gated by $L(\Delta)$, allowing robustness to drift and deliberate trade-offs between interaction time and overlap bandwidth, while retaining a closed-form birth-death description for the cavity photon number. This separation (thermodynamics in the ancilla state, geometry in the two-atom enhancement, and spectroscopy in the detuning filter) offers clear handles for calibration and stability in the lab.[2,7]

Open technical challenges frame the near-term research agenda. Heat loads from rapid qubit resets and control pulses must be budgeted to avoid excess quasiparticles and stray photons; high-isolation, low-loss switching between "engage" and "idle" configurations is needed to maintain the small-angle regime; and Poissonization of cycle timing should be verified so the coarse-grained Lindblad limit applies. Multi-mode crowding in 3D enclosures can be turned from a nuisance into a feature by using engineered filters and parametric couplers to direct entropy flow, but this requires careful microwave design. On the metrology side, QND tools from circuit QED, micromaser-inspired counting statistics and modern bosonic-code diagnostics, can be repurposed to quantify the effective temperature and detailed balance imposed by the ancilla reservoir. Finally, integrating this refrigerator with error-corrected bosonic encodings (cat, binomial, GKP) suggests a route to hardware that both cools and stabilizes logical states at the 1 K tier, leveraging the same reservoir-engineering toolbox demonstrated in recent autonomous QEC experiments.[14,34]

In sum, by combining the high-power 1 K environment with a two-qubit, resettable working medium, the proposed refrigerator creates localized low-entropy regions, T_{cav} in the 50-120 mK range, without relying on the dilution refrigerator's base plate. The collision-model derivation, the experimental maturity of fast reset and autonomous stabilization, and the demonstrated strong coupling to semiconductor nanostructures collectively support a credible path to large-scale, higher-temperature quantum hardware in which refrigeration is delivered where and when it is needed, rather than being globally imposed by the coldest stage.

Conclusion

We have developed a comprehensive theoretical framework for cooling a phonon-tethered microwave cavity using a stream of correlated two-level systems, including realistic phonon environments, detuning filters, finite cavity decay, and both single- and double-atom coupling configurations. By deriving explicit Lindblad-rate equations and analytically tractable steady-state solutions for the cavity photon number, we have shown how the interplay of weak collisions, intra-pair correlations, detuning, and phonon loss determines the nonequilibrium temperature imposed on the cavity. Our results demonstrate that while a single interacting atom in each correlated pair can partially suppress phonon-induced heating, genuine refrigeration, where the cavity is driven below the temperature of the atomic reservoir, requires the

collective interaction of both atoms in the pair. This two-atom configuration harnesses exchange-enhanced correlations and coherence to reshape the effective detailed balance seen by the cavity, producing cooling minima as deep as $T_{\text{cav}}/T_{\text{atom}} \approx 0.5$ under realistic coupling strengths and spectral conditions.

Systematic evaluation of the analytic steady-state expressions across a wide parameter space reveals the operational boundaries of this quantum refrigerator, including its sensitivity to detuning, the crucial role of the cavity–bath leakage rate, and the enhancement provided by strong atom–cavity coupling. The resulting cooling landscapes identify broad regions in which the engineered atomic reservoir can overcome environmental heating and impose a colder nonequilibrium steady state. By comparing the one-atom and two-atom models, we have clarified the qualitative advantages of collective coupling, including stronger refrigeration, wider detuning tolerance, and reduced sensitivity to asymmetries in the thermal weights of the incoming states.

Motivated by these theoretical insights, we have mapped the two-atom cooling mechanism onto a practical cQED architecture. In this platform, two superconducting qubits serve as the working medium, a high-Q 3D cavity provides the target bosonic mode, and fast dissipative or measurement-based resets maintain the qubit pair at an effective temperature far below that of a 1 K cryogenic stage. This experimental mapping connects our theoretical model directly to state-of-the-art techniques in cQED, including Purcell-enhanced reset, parametric sideband interactions, tunable couplers, and intercavity beam-splitters. The combined system offers a realistic pathway for creating local sub–100-mK cold spots inside a warm enclosure, potentially enabling scalable quantum information architectures in which most control electronics reside at high-power cryogenic stages while only selected modes or devices are actively refrigerated via engineered quantum reservoirs.

Overall, this work bridges quantum thermodynamics, collision-model open-system theory, and modern cQED hardware to propose a feasible route toward autonomous cavity cooling far below ambient cryogenic temperatures. The enhanced performance of the two-atom reservoir underscores the central role of quantum correlations in nonequilibrium quantum machines and opens opportunities for integrating similar cooling modules with semiconductor quantum dots, spin qubits, bosonic memories, and other temperature-sensitive quantum devices. Future work may extend this framework to driven dissipative steady-state engineering, multi-mode refrigeration, and autonomous thermal management in large-scale quantum processors.

Acknowledgement

References

[1] Bluefors, "Dilution Refrigerator Measurement System", accessed November 28, 2025, https://bluefors.com/products/dilution-refrigerator-measurement-systems/ld-dilution-refrigerator-measurement-system/.

[2] Bluefors, LDHe Measurement System, accessed November 28, 2025, https://bluefors.com/products/1k-systems/ldhe-measurement-system/.

[3] Uhlig, Kurt. "Dry dilution refrigerator with 4He-1 K-loop." *Cryogenics* 66 (2015): 6-12.

[4] Bluefors, "Introducing the XLDHe High Power System - Ultimate Cooling for 1 K Experiments," accessed November 28, 2025, https://bluefors.com/news/introducing-the-xldhe-high-power-system-ultimate-cooling-for-1-k-experiments/

[5] Bluefors, "XLDHe High Power System," accessed November 28, 2025, https://bluefors.com/products/1k-systems/xldhe-high-power-system

[6] Bluefors, "Introducing the Ultra-Compact Dilution Refrigerator System", accessed November 28, 2025, https://bluefors.com/news/introducing-the-ultra-compact-dilution-refrigerator-system

[7] Bluefors, "LD Dilution Refrigerator Measurement System", , accessed November 28, 2025, https://bluefors.com/products/dilution-refrigerator-measurement-systems/ld-dilution-refrigerator-measurement-system

[8] Krantz, Philip, Morten Kjaergaard, Fei Yan, Terry P. Orlando, Simon Gustavsson, and William D. Oliver. "A quantum engineer's guide to superconducting qubits." *Applied physics reviews* 6, no. 2 (2019).

[9] Blais, Alexandre, Arne L. Grimsmo, Steven M. Girvin, and Andreas Wallraff. "Circuit quantum electrodynamics." *Reviews of Modern Physics* 93, no. 2 (2021): 025005.

[10] Dillenschneider, Raoul, and Eric Lutz. "Energetics of quantum correlations." *Europhysics Letters* 88, no. 5 (2009): 50003.

[11] Gardiner, Crispin W., and Matthew J. Collett. "Input and output in damped quantum systems: Quantum stochastic differential equations and the master equation." *Physical Review A* 31, no. 6 (1985): 3761.

[12] Ciccarello, Francesco, Salvatore Lorenzo, Vittorio Giovannetti, and G. Massimo Palma. "Quantum collision models: Open system dynamics from repeated interactions." *Physics Reports* 954 (2022): 1-70.

[13] Clerk, Aashish A. "Quantum noise and quantum measurement." Quantum Machines: Measurement and Control of Engineered Quantum Systems (2008).

[14] Filipowicz, P., Javanainen, J., & Meystre, P., Theory of a microscopic maser, Phys. Rev. A 34, 3077 (1986)

[15] Linden, Noah, Sandu Popescu, and Paul Skrzypczyk. "How small can thermal machines be? The smallest possible refrigerator." *Physical review letters* 105, no. 13 (2010): 130401.

[16] Correa, Luis A., José P. Palao, Daniel Alonso, and Gerardo Adesso. "Quantum-enhanced absorption refrigerators." *Scientific reports* 4, no. 1 (2014): 3949.

[17] Bhandari, Bibek, and Andrew N. Jordan. "Minimal two-body quantum absorption refrigerator." *Physical Review B* 104, no. 7 (2021): 075442.

[18] Englert, Berthold-Georg. "Elements of micromaser physics." *arXiv preprint quant-ph/0203052* (2002).

[19] Walls, D. F., and Gerard J. Milburn. "Quantum Optics and Quantum Foundations." In *Quantum Optics*, pp. 225-244. Cham: Springer Nature Switzerland, 2025.

[20] Forn-Díaz, P., L. Lamata, E. Rico, J. Kono, and E. Solano. "Ultrastrong coupling regimes of light-matter interaction." *Reviews of Modern Physics* 91, no. 2 (2019): 025005.

[21] Mundada, Pranav, Gengyan Zhang, Thomas Hazard, and Andrew Houck. "Suppression of qubit crosstalk in a tunable coupling superconducting circuit." *Physical Review Applied* 12, no. 5 (2019): 054023.

[22] Campbell, Daniel L., Archana Kamal, Leonardo Ranzani, Michael Senatore, and Matthew D. LaHaye. "Modular tunable coupler for superconducting circuits." *Physical Review Applied* 19, no. 6 (2023): 064043.

[23] Magnard, Paul, Philipp Kurpiers, Baptiste Royer, Theo Walter, J-C. Besse, Simone Gasparinetti, Marek Pechal et al. "Fast and unconditional all-microwave reset of a superconducting qubit." *Physical review letters* 121, no. 6 (2018): 060502.

[24] Ristè, D., C. C. Bultink, Konrad W. Lehnert, and L. DiCarlo. "Feedback control of a solid-state qubit using high-fidelity projective measurement." *Physical review letters* 109, no. 24 (2012): 240502.

[25] Shankar, S., M. Hatridge, Z. Leghtas, K. M. Sliwa, A. Narla, U. Vool, S. M. Girvin, L. Frunzio, M. Mirrahimi, and M. H. Devoret. "Stabilizing entanglement autonomously between two superconducting qubits." *arXiv preprint arXiv:1307.4349* (2013).

[26] Gu, Xu-Yang, Da'er Feng, Zhen-Yu Peng, Gui-Han Liang, Yang He, Yongxi Xiao, Ming-Chuan Wang et al. "Engineering a Multi-Mode Purcell Filter for Superconducting-Qubit Reset and Readout with Intrinsic Purcell Protection." *arXiv preprint arXiv:2507.04676* (2025).

[27] Sunada, Yoshiki, Shingo Kono, Jesper Ilves, Shuhei Tamate, Takanori Sugiyama, Yutaka Tabuchi, and Yasunobu Nakamura. "Fast readout and reset of a superconducting qubit coupled to a resonator with an intrinsic Purcell filter." *Physical Review Applied* 17, no. 4 (2022): 044016.

[28] Ding, Jiayu, Yulong Li, He Wang, Guangming Xue, Tang Su, Chenlu Wang, Weijie Sun et al. "Multipurpose architecture for fast reset and protective readout of superconducting qubits." *Physical Review Applied* 23, no. 1 (2025): 014012.

[29] Reed, Matthew D., Blake R. Johnson, Andrew A. Houck, Leonardo DiCarlo, Jerry M. Chow, David I. Schuster, Luigi Frunzio, and Robert J. Schoelkopf. "Fast reset and suppressing spontaneous emission of a superconducting qubit." *Applied Physics Letters* 96, no. 20 (2010).

[30] Alhambra, Álvaro M., Matteo Lostaglio, and Christopher Perry. "Heat-bath algorithmic cooling with optimal thermalization strategies." *Quantum* 3 (2019): 188.

[31] Zhou, Yu, Zhenxing Zhang, Zelong Yin, Sainan Huai, Xiu Gu, Xiong Xu, Jonathan Allcock et al. "Rapid and unconditional parametric reset protocol for tunable superconducting qubits." *Nature Communications* 12, no. 1 (2021): 5924.

[32] Shah, Parth S., Frank Yang, Chaitali Joshi, and Mohammad Mirhosseini. "Stabilizing remote entanglement via waveguide dissipation." *PRX Quantum* 5, no. 3 (2024): 030346.

[33] Li, Ziqian, Tanay Roy, Yao Lu, Eliot Kapit, and David I. Schuster. "Autonomous stabilization with programmable stabilized state." *Nature Communications* 15, no. 1 (2024): 6978.

[34] Lachance-Quirion, Dany, Marc-Antoine Lemonde, Jean Olivier Simoneau, Lucas St-Jean, Pascal Lemieux, Sara Turcotte, Wyatt Wright et al. "Autonomous quantum error correction of Gottesman-Kitaev-Preskill states." *Physical Review Letters* 132, no. 15 (2024): 150607.

[35] Stockklauser, Anna, Pasquale Scarlino, Jonne V. Koski, Simone Gasparinetti, Christian Kraglund Andersen, Christian Reichl, Werner Wegscheider, Thomas Ihn, Klaus Ensslin, and Andreas Wallraff. "Strong coupling cavity QED with gate-defined double quantum dots enabled by a high impedance resonator." *Physical Review X* 7, no. 1 (2017): 011030.

[36] Mi, Xiao, J. V. Cady, D. M. Zajac, P. W. Deelman, and Jason R. Petta. "Strong coupling of a single electron in silicon to a microwave photon." *Science* 355, no. 6321 (2017): 156-158.

[37] Sirois, Adam J., M. A. Castellanos-Beltran, M. P. DeFeo, L. Ranzani, F. Lecocq, R. W. Simmonds, J. D. Teufel, and J. Aumentado. "Coherent-state storage and retrieval between superconducting cavities using parametric frequency conversion." *Applied Physics Letters* 106, no. 17 (2015).

[38] Chapman, Benjamin J., Stijn J. De Graaf, Sophia H. Xue, Yaxing Zhang, James Teoh, Jacob C. Curtis, Takahiro Tsunoda et al. "High-on-off-ratio beam-splitter interaction for gates on bosonically encoded qubits." *PRX Quantum* 4, no. 2 (2023): 020355.

[39] Cai, Weizhou, Yuwei Ma, Weiting Wang, Chang-Ling Zou, and Luyan Sun. "Bosonic quantum error correction codes in superconducting quantum circuits." *Fundamental Research* 1, no. 1 (2021): 50-67.

[40] Underwood, Devin, Joseph A. Glick, Ken Inoue, David J. Frank, John Timmerwilke, Emily Pritchett, Sudipto Chakraborty et al. "Using cryogenic CMOS control electronics to enable a two-qubit cross-resonance gate." *PRX Quantum* 5, no. 1 (2024): 010326.

[41] Pellerano, Stefano, Sushil Subramanian, Jong-Seok Park, Bishnu Patra, Todor Mladenov, Xiao Xue, Lieven MK Vandersypen, Masoud Babaie, Edoardo Charbon, and Fabio Sebastiano. "Cryogenic CMOS for qubit control and readout." In *2022 IEEE Custom Integrated Circuits Conference (CICC)*, pp. 01-08. IEEE, 2022.

[42] Gross, Michel, and Serge Haroche. "Superradiance: An essay on the theory of collective spontaneous emission." *Physics reports* 93, no. 5 (1982): 301-396.

[43] Dicke, Robert H. "Coherence in spontaneous radiation processes." *Physical review* 93, no. 1 (1954): 99.

[44] Poyatos, J. F., J. Ignacio Cirac, and P. Zoller. "Quantum reservoir engineering with laser cooled trapped ions." *Physical review letters* 77, no. 23 (1996): 4728.

[45] Poyatos, J. F., J. Ignacio Cirac, and P. Zoller. "Quantum reservoir engineering with laser cooled trapped ions." *Physical review letters* 77, no. 23 (1996): 4728.

[46] Ding, Leon, Max Hays, Youngkyu Sung, Bharath Kannan, Junyoung An, Agustin Di Paolo, Amir H. Karamlou et al. "High-fidelity, frequency-flexible two-qubit fluxonium gates with a transmon coupler." *Physical Review X* 13, no. 3 (2023): 031035.

[47] Gargiulo, O., S. Oleschko, J. Prat-Camps, M. Zanner, and G. Kirchmair. "Fast flux control of 3D transmon qubits using a magnetic hose." *Applied Physics Letters* 118, no. 1 (2021).

[48] Han, Lian-Chen, Yu Xu, Jin Lin, Fu-Sheng Chen, Shao-Wei Li, Cheng Guo, Na Li et al. "Active reset of superconducting qubits using the electronics based on RF switches." *AIP Advances* 13, no. 9 (2023).

[49] Serafini, A., M. Lostaglio, S. Longden, U. Shackerley-Bennett, C-Y. Hsieh, and G. Adesso. "Gaussian thermal operations and the limits of algorithmic cooling." *Physical Review Letters* 124, no. 1 (2020): 010602.

[50] Vashaee, Daryoosh, and Jahanfar Abouie. "Microwave-induced cooling in double quantum dots: Achieving millikelvin temperatures to reduce thermal noise around spin qubits." *Physical Review B* 111, no. 1 (2025): 014305.